Carbon dioxide snow clouds on Mars: South polar winter observations by the Mars Climate Sounder

Paul O. Hayne,[1,2] David A. Paige,[2] John T. Schofield,[3] David M. Kass,[3] Armin Kleinböhl,[3] Nicholas G. Heavens,[4] and Daniel J. McCleese[3]

Received 16 December 2011; revised 7 May 2012; accepted 11 July 2012; published 29 August 2012.

[1] We present south polar winter infrared observations from the Mars Climate Sounder (MCS) and test three hypotheses concerning the origins of "cold spots": regions of anomalously low infrared brightness temperatures, which could be due to enrichment in non-condensable gases, low-emissivity surface frost, or optically thick CO_2 clouds. Clouds and surface frosts have been historically difficult to distinguish, but the unique limb sounding capability of MCS reveals extensive tropospheric CO_2 clouds over the cold spots. We find that both clouds and surface deposits play a significant role in lowering the infrared emissivity of the seasonal ice cap, and the granular surface deposits are likely emplaced by snowfall. Surface temperatures indicate the polar winter atmosphere is enriched by a factor ~5–7 in non-condensable gases relative to the annual average, consistent with earlier gamma ray spectrometer observations, but not enough to account for the low brightness temperatures. A large ~500-km diameter cloud with visible optical depth ~0.1–1.0 persists throughout winter over the south polar residual cap (SPRC). At latitudes 70–80°S, clouds and low emission regions are smaller and shorter-lived, probably corresponding to large-grained "channel 1" clouds observed by the Mars Orbiter Laser Altimeter. Snowfall over the SPRC imparts the lowest emissivity in the south polar region, which paradoxically tends to reduce net accumulation of seasonal CO_2 by backscattering infrared radiation. This could be compensated by the observed anomalously high summertime albedo of the SPRC, which may be related to small grains preserved in a rapidly formed snow deposit.

Citation: Hayne, P. O., D. A. Paige, J. T. Schofield, D. M. Kass, A. Kleinböhl, N. G. Heavens, and D. J. McCleese (2012), Carbon dioxide snow clouds on Mars: South polar winter observations by the Mars Climate Sounder, *J. Geophys. Res.*, *117*, E08014, doi:10.1029/2011JE004040.

1. Introduction

[2] One of the more prominent features of the Martian climate is the seasonal exchange of carbon dioxide between the atmosphere and surface. During winter, a substantial portion of the atmosphere freezes out, forming the seasonal ice caps and reducing surface pressures globally. Summertime sublimation replenishes atmospheric CO_2 as the seasonal cap recedes toward the pole, with a perennial carbon dioxide deposit persisting only in the southern hemisphere [*Kieffer*, 1979]. Pressure variations measured by the Viking landers in the 1970s confirmed that as much as 30% of the atmosphere participates in this annual CO_2 cycle [*James et al.*, 1992]. The existence of this cycle and its effect on atmospheric pressures had been predicted by *Leighton and Murray* [1966] on the basis of a polar energy balance model. The success of their model proved that atmospheric pressure on Mars is largely controlled by the polar energy balance on seasonal and annual time scales. During summer, insolation is balanced against infrared emission and the latent heat of subliming CO_2, as well as conductive heat exchange with the subsurface. Winter on Mars brings "polar night" to latitudes poleward of roughly 65°, when the sun remains continuously below the horizon for one or more days. During this period, the atmosphere and surface cool by infrared emission to space until atmospheric carbon dioxide begins to condense, at which point further cooling is buffered by the release of latent heat. Advective transport of heat into the polar regions is inefficient due to the low density of the Martian atmosphere. Leighton and Murray noted that to first order, the amount of carbon dioxide condensing during polar night can therefore be estimated from the net outgoing infrared flux, which should be approximately equal to the

[1]Division of Geological and Planetary Sciences, California Institute of Technology, Pasadena, California, USA.
[2]Earth and Space Sciences Department, University of California, Los Angeles, California, USA.
[3]NASA Jet Propulsion Laboratory, California Institute of Technology, Pasadena, California, USA.
[4]Earth and Atmospheric Sciences, Cornell University, Ithaca, New York, USA.

Corresponding author: P. O. Hayne, Division of Geological and Planetary Sciences, California Institute of Technology, Pasadena, CA 91125 (phayne@gps.caltech.edu)

0148-0227/12/2011JE004040

blackbody emission of a ~145 K solid CO_2 cap in vapor pressure equilibrium with the atmosphere.

[3] Despite the initial success of Leighton and Murray's energy balance approach, no model has yet succeeded in predicting both the seasonal pressure cycle and the existence of the perennial CO_2 cap near the south pole. Part of the problem may be that the polar caps exhibit infrared emission far from the expected blackbody behavior; regions of very low thermal emission in the polar night have been observed from orbit since the Viking era [*Kieffer et al.*, 1976]. Within these widespread low emission regions (a.k.a. "cold spots"), 20-μm brightness temperatures are up to 30 K below the expected frost point temperature [*Titus et al.*, 2001]. Such large reductions in infrared emission have a measurable influence on seasonal and interannual pressure variations on Mars by altering the polar energy balance [*Paige and Ingersoll*, 1985], but the cause of this phenomenon is not well understood. Three primary hypotheses were proposed by *Kieffer et al.* [1976, 1977] to explain the low emission regions:

[4] 1. Depletion of CO_2 relative to non-condensing gases (mostly N_2 and Ar) lowers the equilibrium temperature of the ice cap.

[5] 2. Carbon dioxide ice clouds backscatter infrared radiation emitted by the surface.

[6] 3. Surface frosts on the seasonal ice caps have intrinsically low infrared emissivity.

[7] While all three explanations are generally consistent with existing observations, fine-grained surface frost and CO_2 clouds are considered to be most likely, because dynamical instability prevents local depletion of CO_2 gas to the extent required to lower the frost point more than a few degrees [*Hess*, 1979; *Weiss and Ingersoll*, 2000]. Nadir-looking infrared observations of low emission regions by the Mariner and Voyager spacecraft seem to be equally consistent with scattering by optically thick CO_2 clouds or fine-grained (<1 mm) surface frosts, offering no conclusive distinction between the two [*Forget et al.* 1995, 1998]. More recent observations by the Mars Global Surveyor Thermal Emission Spectrometer (TES) revealed low emission regions occurring under a clear atmosphere, consistent with surface frost or freshly fallen snow [*Hansen*, 1999], yet others occurred under a supersaturated atmosphere, suggesting the presence of clouds [*Titus et al.*, 2001]. Atmospheric reflections commonly observed within the polar night by the Mars Orbiter Laser Altimeter (MOLA) have been attributed to optically thick CO_2 clouds, but their composition and precipitation rates could not be directly constrained [*Neumann et al.*, 2003; *Colaprete et al.*, 2003]. Despite this tantalizing evidence, carbon dioxide snow clouds have been historically difficult to observe, because thermodynamic conditions favorable to their formation exist only in the darkness of polar night [*Gierasch and Goody*, 1968], and traditional nadir-looking infrared remote sensing cannot distinguish them from surface deposits [*Forget et al.*, 1995].

[8] Uncovering the nature of low emission regions has many repercussions for our understanding of the Martian carbon dioxide cycle and its role in regulating the planet's climate. Snowfall can affect the polar energy budget in both direct and indirect ways, first as clouds backscatter outgoing infrared radiation [*Hunt*, 1980], and second as snow grains reaching the surface reduce the emissivity of the seasonal ice caps [*Ditteon and Kieffer*, 1979]. While fine-grained frost deposited directly at the surface is expected to undergo rapid sintering, somewhat larger snow grains may persist unaltered for the entire season [*Clark et al.*, 1983; *Eluszkiewicz*, 1993]. If the granularity of a snow deposit is preserved until springtime, its higher reflectivity compared to a nonporous "slab ice" deposit may reduce its net sublimation – a potential prerequisite for maintaining a perennial CO_2 cap [*Jakosky and Haberle*, 1990; *Kieffer et al.*, 2000; *Titus et al.*, 2001]. In this way, the mode of carbon dioxide deposition could affect the polar energy balance on annual or even interannual timescales.

[9] New observations by the Mars Climate Sounder provide the first opportunity to directly witness the condensing seasonal polar caps and atmosphere in three dimensions. In fact, the MCS Science Team noted tantalizing evidence of CO_2 clouds over the winter pole very early in the investigation (J. T. Schofield, personal communication, 2006), which motivated further study. We begin this paper with a description of the MCS instrument and the data set used in this study, and predicted emission spectra of clouds and frosts. Then we present the south polar winter observations, focusing on the general radiative properties relevant for understanding the nature of low emission regions. Finally, we test the cloud and surface frost hypotheses through a combination of MCS observations and radiative transfer models.

2. Instrumentation and Data

2.1. Mars Climate Sounder

[10] The Mars Climate Sounder (MCS) is a multispectral visible and infrared filter radiometer onboard the Mars Reconnaissance Orbiter (MRO), which began its science phase in November of 2006. One of the primary goals motivating the design of the MCS investigation was probing the energy balance of the polar regions [*McCleese et al.*, 2007]. The instrument has nine channels spanning the wavelength range ~0.3–45 μm (33,000–220 cm^{-1}), with one visible and eight IR channels. An important capability of MCS is independent two-axis scanning, which allows the telescopes to view either the limb (typically forward in the orbit track), or nadir. Each spectral channel consists of a linear array of 21 thermopile detectors, each with a field of view (FOV) of ~3.6 × 6.1 mrad, corresponding to a typical vertical limb resolution of ~5 km, and a surface resolution of ~1 km (though spacecraft motion typically smears this resolution to ~6 km on the surface). In the limb sounding mode, the detectors' shorter dimension is oriented vertically, with the 21 detectors spanning limb tangent points from the surface up to ~90 km altitude. Within about 5 km of the surface, radiance contamination by high-angle emission from the Martian surface prevents accurate retrieval of aerosol opacity from limb tangent measurements.

[11] The standard pipeline calibration procedures for MCS are described in its Reduced Data Record Software Interface Specification [*Henderson and Sayfi*, 2007], which is publicly available in the NASA Planetary Data System. Measured voltages are converted to spectral radiance, in units of mW m^{-2} sr^{-1} cm, with an uncertainty of approximately ±0.5% in radiance [*McCleese et al.*, 2007; *Kleinböhl et al.*, 2009]. Frequent calibrations ensure that the accuracy of all calibrated brightness temperature measurements is better than ±0.25 K at 300 K, and less than ±1 K at 150 K (Table 1). Thus the measurement error is dominated by the

Table 1. Aerosol Optical Properties and MCS Channels Used in This Study

	Channel	A4	A5	B1
	λ (μm)	11.87	21.90	32.79
	ν (cm^{-1})	842.5	456.6	305
	ΔT_{NE} (K) at 150 K	0.46	0.13	0.81
Q_{ext}	CO_2 (r_{eff} = 1 μm)	0.0226	0.0027	0.0006
	CO_2 (r_{eff} = 10 μm)	3.5171	3.0249	2.4851
	CO_2 (r_{eff} = 100 um)	2.1362	2.2057	2.2732
	H_2O (r_{eff} = 1.0 um)	0.7730	0.0515	0.0759
	Dust (r_{eff} = 1.5 um)	0.2747	0.3506	0.1777
ϖ_0	CO_2 (r_{eff} = 1 μm)	0.9873	0.9947	0.9300
	CO_2 (r_{eff} = 10 μm)	0.9985	0.9998	0.9985
	CO_2 (r_{eff} = 100 um)	0.9796	0.9983	0.9967
	H_2O (r_{eff} = 1.0 um)	0.1074	0.2545	0.0180
	Dust (r_{eff} = 1.5 um)	0.4419	0.0550	0.0332
g	CO_2 (r_{eff} = 1 μm)	0.0900	0.0278	0.0125
	CO_2 (r_{eff} = 10 μm)	0.7880	0.7536	0.7272
	CO_2 (r_{eff} = 100 um)	0.8384	0.7943	0.7794
	H_2O (r_{eff} = 1.0 um)	0.2399	0.0979	0.0413
	Dust (r_{eff} = 1.5 um)	0.3122	0.1056	0.0611

intrinsic instrument noise at signal levels of interest. In all of the observations presented in this paper, spectral radiances I_ν have been converted to equivalent brightness temperatures using each channel's effective center frequency ν. In the radiative transfer calculations, we integrate monochromatic radiances line-by-line over the full spectral response of each MCS channel [*McCleese et al.*, 2007], and then convert these to an equivalent brightness temperature via a lookup table generated by convolution of the spectral response with blackbody emission curves. Following convention, we denote brightness temperatures by T_λ, where λ is the channel's effective center wavelength. Wherever we combined multiple observations to create maps or profiles, we typically averaged radiance values first, and then converted to brightness temperature. This procedure is necessary to properly account for the noise statistics, especially at low temperatures and for the longer wavelength B-channels.

2.2. Data Set

[12] Several Mars years are spanned by the MCS investigation. Good wintertime data are available for both poles, with the best on-planet data set during the southern winter of Mars Year 28 (A.D. 2006–2007, following the convention of *Clancy et al.* [2000]). In this paper, we focus mainly on a subset of MCS nadir observations at the start of the MRO mission, spanning the range L_S = 110°–150° (where L_S is the areocentric solar longitude, defined by L_S = 0° for northern spring equinox), encompassing most of the southern winter season. The extremely short radiative cooling time of the Martian atmosphere (typically less than one sol) dictates that the coldest day of the year in the polar regions always occurs near winter solstice (L_S = 90° in the South). After this instant of minimum insolation, sunlight begins creeping poleward. By L_S = 180° the south pole receives its first grazing photons. Thus, the south polar study period starts near the coldest day of the year and ends as spring begins to set in.

[13] During the south polar winter study period, MCS acquired both nadir and limb observations, with good spatial and temporal overlap. Nadir data over the polar regions were acquired during MY28 using a "buckshot" strategy, where the instrument rapidly scanned to many different angles to get the best possible spatial and emission angle coverage, including latitudes >87° where most nadir-looking instruments have data gores. Identifying each measurement with a spatial bin involves calculating intersection points for "on-planet" views, and tangent points for "off-planet" views, from the more primitive spacecraft geometry and MCS look angles. At a typical spacecraft altitude over the south polar region of ~250 km, the full-width at half-max (FWHM) of the detector field of view response (~3.6 × 6.2 mrad) projects onto a surface element with dimensions ~1.0 × 1.5 km. For off-nadir measurements, the FOV surface projection grows, as do errors due to topography. Restricting the emission angle θ < 70°, the typical south polar RMS topographic relief of $\Delta h \sim 1$ km on a ~4 km length scale (derived from the MOLA 16 pixel-per-degree grid [*Smith et al.*, 2001]), introduces horizontal errors $\Delta h \tan\theta < 2.5$ km; by comparison, the FOV projection is <5 km. Spacecraft motion smears the on-planet footprint to ~6 km when pointed to true nadir, with smearing becoming less important at higher emission angles.

[14] Localizing limb tangent points to a position on the surface carries some uncertainty due to the finite detector field of view, and atmospheric properties. The extent of tangent points sampled is given by the convolution of each detector's field of view response with appropriate spatial weighting functions, which depend on the composition and distribution of gas and aerosols in the atmosphere. In the limit of a homogeneous, spherically symmetric atmosphere, a vertical resolution of Δz corresponds to a range along the line of sight $\Delta x \approx 2\sqrt{R\Delta z}$, where R is the planetary radius. For a typical vertical resolution at the limb of ~5 km [*Kleinböhl et al.*, 2009], the line-of-sight range in tangent points sampled is then ~260 km. Spatial uncertainties perpendicular to the line of sight are expected to be comparable to this extent, owing to the opposing effects of the slightly larger horizontal FOV (~8 km) and lower densities sampled by points away from the line of sight. We note, however, that whenever clouds are optically thick in the line of sight, the horizontal weighting functions are no longer peaked at the tangent altitude, introducing further uncertainty. Nonetheless, opacity retrievals show the clouds are not typically opaque along the line of sight (section 4.4).

[15] Using nadir infrared measurements from TES, *Cornwall and Titus* [2010] cataloged the sizes and decay times for south polar "cold spots" within the zonal band 86 to 87.2°S, finding typical diameters in the range ~60–160 km. In an attempt to identify individual cold spots in this size range, we averaged both the MCS limb and nadir measurements in ~60 × 60 km bins (~1° latitude square at the pole). Typical coverage in the polar regions (60°–90° latitude) is ~5–20 limb and ~5–20 nadir observations per channel per sol per bin for the south polar winter study period. Given the uncertainties in limb tangent positions, however, we expect limb measurements binned at <300 km to contain significant "noise" due to the course spatial resolution of these measurements, especially if sub-pixel clouds are varying more rapidly than our temporal bin size of ~1 sol.

3. Radiative Properties of CO_2 Clouds and Frosts

[16] Emission spectra measured by MCS at the top of the atmosphere depend on the optical properties of the surface, as well as scattering by clouds and aerosols in the atmosphere.

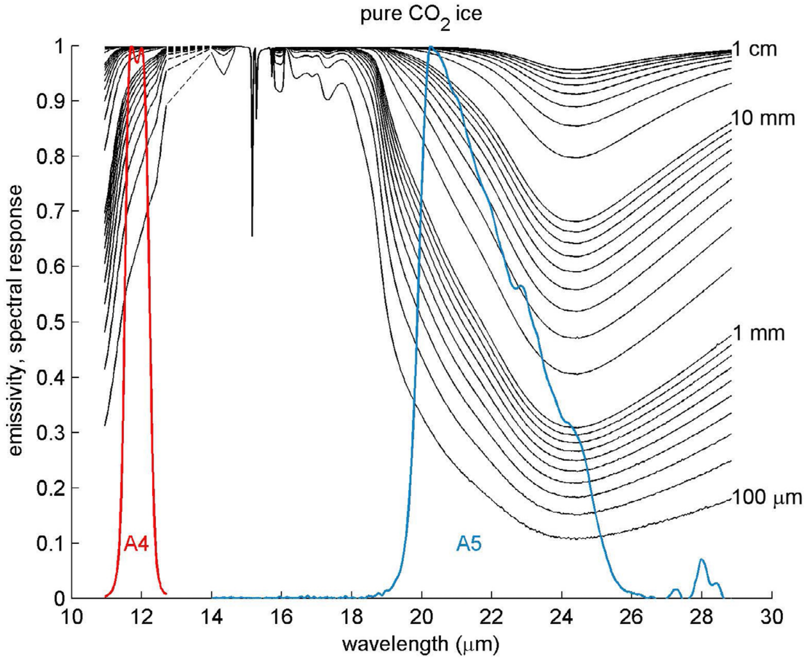

Figure 1. Emissivity spectra for pure CO_2 deposits using optical constants from *Hansen* [1997] and the albedo model of *Wiscombe and Warren* [1980]. Normalized MCS spectral response functions for channels A4 (12 μm) and A5 (22 μm) are shown for reference. Channel A5 samples the 25-μm transparency band of granular carbon dioxide ice, while A4 is near the shoulder of the 15-μm emissivity maximum.

Both clouds and surface frosts may contribute to the reduced infrared brightness temperatures [e.g., *Hansen*, 1999]. Distinguishing between clouds and surface frosts is facilitated by the unique capability of MCS to acquire both limb and nadir measurements of low emission regions. We begin by modeling the infrared emission of clouds and surface frosts for a range of grain sizes and cloud optical depths. These models can then be compared to the MCS nadir measurements, which provide constraints on the range of possible grain sizes and optical depths of the clouds or frosts responsible for the observed low emission regions. Finally, we retrieve cloud optical depths from the limb measurements, lending insight into the relative importance of frosts and clouds in reducing infrared emission from the south polar seasonal cap.

3.1. Carbon Dioxide Frosts in the Infrared

[17] On airless bodies, infrared emissivity spectra are particularly diagnostic of composition and particle size [e.g., *Hapke*, 1993; *Clark*, 1999]. From previous infrared measurements during cloud-free periods, the Martian seasonal caps are known to be composed primarily of carbon dioxide ice, mixed with small quantities of dust and water ice "contaminants" [*Hansen*, 1999]. Laboratory and remote infrared measurements of solid CO_2 reveal a broad transparency feature near 25 μm wavelength where a lack of active vibrational modes causes extinction to be dominated by volume scattering [*Ditteon and Kieffer*, 1979]. Because the MCS 22 μm (A5) channel is near the center of this emissivity minimum, the brightness temperature contrast T_{12}–T_{22} is generally expected to be positive for surface deposits of solid CO_2 containing voids or internal facets. Within coarse-grained CO_2 deposits mean photon path lengths are large, allowing radiation to escape from greater depths, which brings emissivity closer to unity. Conversely, volume scattering events are more frequent for fine-grained deposits, resulting in lower emissivity in the transparency band. Thus, T_{12}–T_{22} is diagnostic of CO_2 ice grain size or porosity [*Eluszkiewicz et al.*, 2005]. As a measurement of the depth of the transparency band of solid CO_2, the T_{12}–T_{22} spectral contrast is similar to the "cold spot index" T_{18}–T_{25} used by *Titus et al.* [2001] (also *Cornwall and Titus* [2009]) to identify low emission regions with the Thermal Emission Spectrometer (TES) onboard the Mars Global Surveyor.

[18] We simulated the infrared emission of the seasonal cap using the δ-Eddington model for snowpack albedo by *Wiscombe and Warren* [1980], and single-scattering parameters calculated from Mie theory [e.g., *Hansen and Travis*, 1974], using optical constants from laboratory experiments by *Hansen* [1997]. Figure 1 compares the spectral behavior of a pure, granular CO_2 ice deposit for a range of grain sizes to the response functions for the 12 μm and 22 μm MCS channels, illustrating the expected strong spectral contrast, especially for fine grain sizes. We assumed particle sizes follow the modified gamma distribution [*Deirmendjian*, 1969]:

$$n(r) \sim r^a e^{-br^c}, \tag{1}$$

with a = 2, c = 0.5, and $b = a/cr_m^c$, where r_m is the mode radius. For calculations involving dust we used optical constants from *Wolff et al.* [2006] and also adopted their value r_m = 0.24 μm (optical effective radius r_{eff} = 1.5 μm) derived from dust scattering measurements from MGS-TES and MiniTES on the Mars Exploration Rovers. Water ice particle size distribution parameters were chosen to match those of *Forget et al.* [1995], with a = 3, c = 4.0,

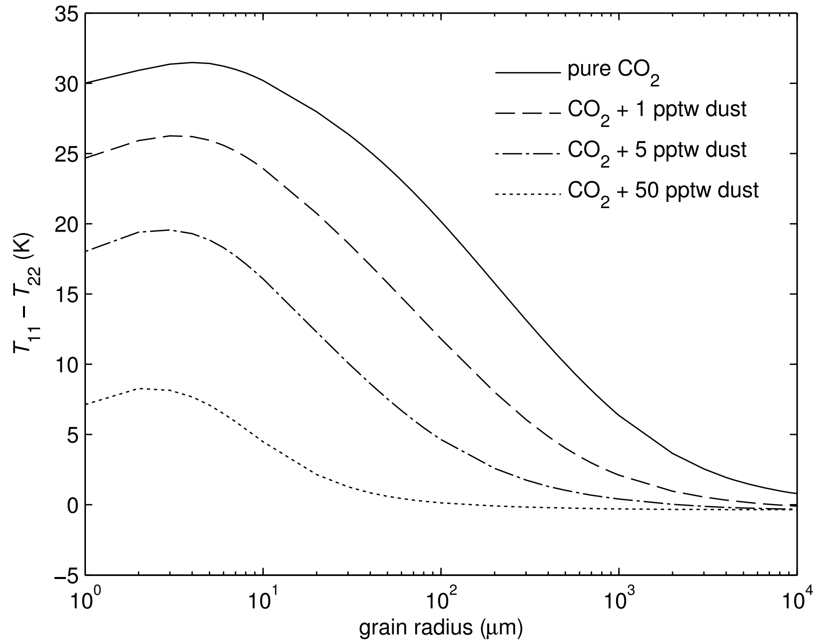

Figure 2. Modeled spectral contrast in the MCS A4 and A5 channels for a range of effective grain radii and dust concentrations given in parts per thousand by weight.

r_m = 0.75 μm (r_{eff} = 1.0 μm), with optical constants from *Warren and Brandt* [2008].

[19] Convolving the response functions for the MCS 12 μm and 22 μm channels with the theoretical spectra in Figure 1 illustrates the dependence of T_{12}–T_{22} on CO_2 grain size (Figure 2). Fine-grained deposits exhibit the highest contrast, with the peak spectral contrast of ~33 K for pure CO_2 occurring for a size distribution with mode radius ~5 μm. Pure CO_2 deposits with mode grain radii >5 mm should not have a measurable spectral contrast, and will therefore appear as blackbody "slab ice" in the absence of clouds [cf. *Kieffer et al.*, 2000]. Scattering parameters of mixtures are assumed to follow $f_{mix} = \sum Q_i r_i^2 n_i f_i / \sum Q_i r_i^2 n_i$, where Q_i is the extinction efficiency, r_i the particle radius, and n_i the number density of the i^{th} species [*Hapke*, 1993, p. 280]. Contamination of the surface deposit by dust tends to reduce the spectral contrast and water frost has a similar diluting effect, though somewhat less than that of dust at the same concentration.

3.2. Carbon Dioxide Ice Clouds in the Infrared

[20] Carbon dioxide ice particles within a cloud emit and scatter radiation emitted by the surface, increasing the spectral contrast T_{12}–T_{22} with increasing optical thickness [*Hunt*, 1980]. In order to calculate the magnitude of this effect, we used a two-stream δ-Eddington radiative transfer model based on that of *Joseph et al.* [1976] and adapted for the infrared (see Appendix A). We calculated Mie parameters for a range of particle compositions and size distribution parameters and forward-modeled clouds of appropriate optical depth, with a typical south polar temperature profile retrieved by MCS during the same season [*Kleinböhl et al.*, 2009]. Figure 3 illustrates the dependence of spectral contrast on a pure carbon dioxide ice cloud's total normal optical depth, for size distributions strongly peaked at 10 and 100 μm. Spectral contrast rises rapidly with increasing optical depth, reaching values of T_{12}–$T_{22} \approx 4$ K, typical for the high latitudes (cf. Figure 4b) near $\tau_{vis} \approx 1$. At very high optical depths the optical properties of the cloud approach those of surface frost, in which case large spectral contrast values may occur even if the surface below consists of slab ice. In the lower atmosphere, where temperatures might permit CO_2 condensation [*Kleinböhl et al.*, 2009], the nadir-measured spectral contrast is fairly insensitive to the altitude of greatest cloud opacity, due to the weak dependence of the CO_2 frost point on pressure.

[21] The results of this section illustrate the fundamental difficulty in using nadir infrared measurements to distinguish between CO_2 clouds and surface frosts. Under the assumption that infrared scattering events are widely separated compared to the wavelength, radiative transfer within an optically thick cloud is essentially the same as if the particles comprising the cloud were instead grains in a surface deposit; although scattering events occur on a much smaller distance scale in the surface deposit, this difference has no effect on the measured radiance. For this reason, coincident limb measurements are vital to distinguishing clouds from surface frosts.

4. Observations

[22] In this section, we present an overview of MCS nadir and limb tangent observations acquired in the Martian south polar winter of MY28. One of the primary goals of this investigation is to quantify the relationship between CO_2 clouds and low infrared emission regions. We therefore begin by identifying low emission regions in the MCS nadir data, and compare their spectra to those observed by previous infrared investigations. Coincident limb measurements by MCS then allow us to quantify atmospheric opacity and test for correlation between clouds and low emission regions.

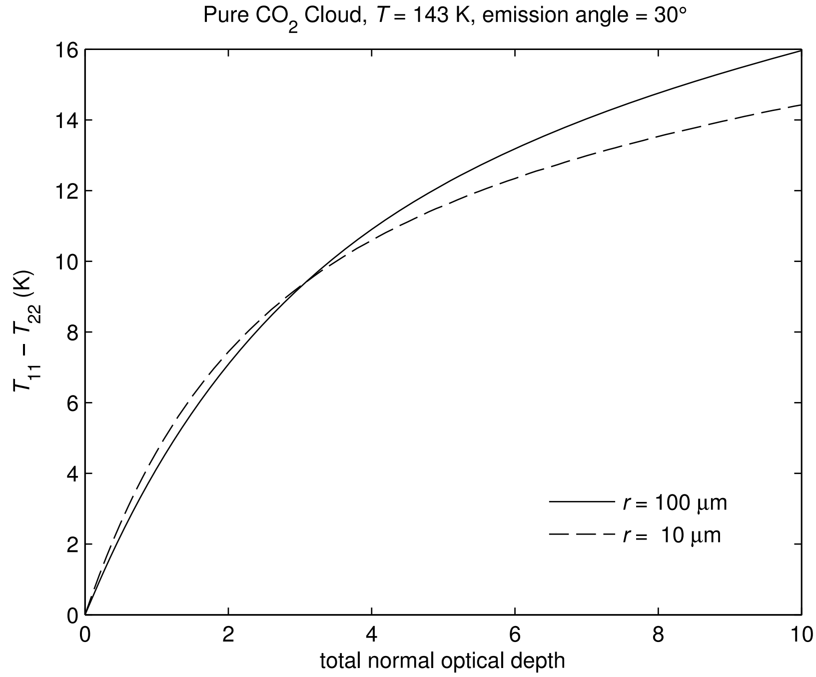

Figure 3. Spectral contrast T_{12}–T_{22} resulting from scattering by a CO_2 cloud as a function of visible optical depth.

4.1. Nadir Observations

[23] A uniform blackbody surface radiating to space under a transparent atmosphere has no spectral contrast, regardless of its thermodynamic temperature or the spectral region sampled. In that case, the emissivity spectrum is uniform and T_{12}–T_{22} = 0. This situation applies to the Mars seasonal CO_2 ice caps only if the deposit is highly nonporous "slab ice," and the atmosphere is effectively transparent in the spectral region sampled [*Kieffer et al.*, 2000; *Titus et al.*, 2001]. In reality, even under a clear sky the infrared emissivity spectrum of the seasonal caps can be complex, indicating

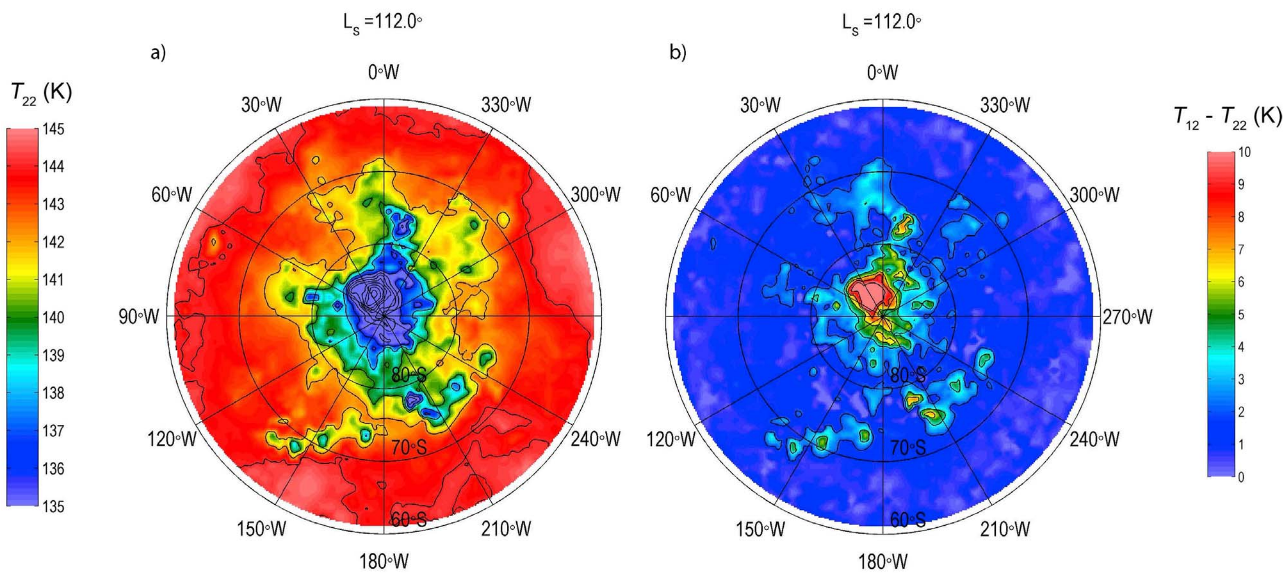

Figure 4. (left) Map of 22-μm brightness temperatures for the south polar winter study region, averaged over 1° L_S (~2 sols) during mid-southern winter (L_S = 112°), with black contours every 2 K. (right) Map of the brightness temperature difference T_{12}–T_{22} for the same period. Black contours indicate each 2 K level from 2–10 K. Positive values correspond to fine-grained surface deposits or clouds of CO_2 ice, where a value of 10 K corresponds to ~1 mm sized grains (see Figure 2) and the spectral contrast tends toward zero for grains larger than ~1 cm. The high-contrast structure near (87°S, 30°W) sits on top of the south polar residual cap (SPRC).

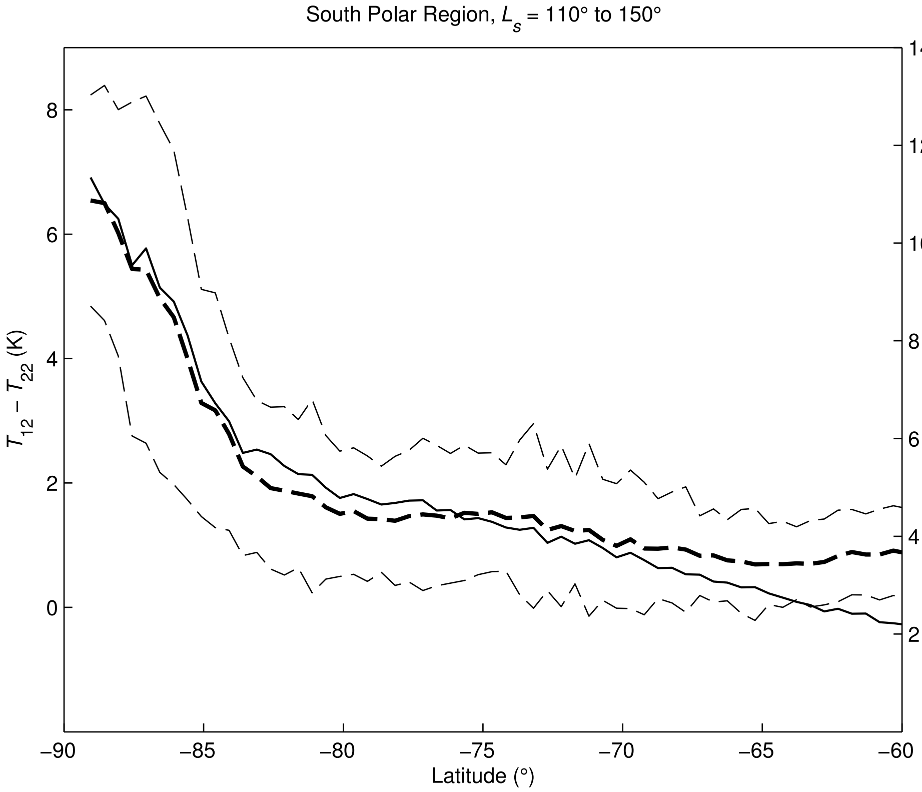

Figure 5. Seasonal average spectral contrast T_{12}–T_{22} values for the south polar winter (thick dashed line), with thin dashed lines indicating the standard deviation within each 0.5-degree latitude bin. The solid line indicates the difference between the local (zonally averaged) CO_2 frost point and the measured nadir brightness temperature in the MCS A5 channel centered at 22 μm.

absorption and scattering by CO_2 grains smaller than ~1 cm, which have been shown to correlate with regions of low integrated infrared emission in earlier data sets [e.g., *Forget et al.*, 1995]. As shown in section 3, the contrast T_{12}–T_{22} can be used as a proxy for the effective grain size of a surface CO_2 deposit when the atmosphere is clear, with higher contrast ($T_{12} > T_{22}$) indicating smaller grains [cf. *Hansen*, 1999]. Figure 4 shows the typical mid-southern winter thermal emission measured by MCS, illustrating the abundance and complex distribution of low emission regions. Over the great majority of the polar winter CO_2 caps, T_{12}–T_{22} < 2 K, indicating that slab ice may dominate the seasonal cap by area, especially at latitudes <80°S (cf. springtime measurements by *Langevin et al.* [2006]). Sporadic fluctuations typically occurring on time scales of one Martian day also produce large positive values of T_{12}–T_{22} locally, and large negative values are seldom, if ever seen during polar night. The region poleward of 80°S consistently has the highest values of T_{12}–T_{22}, consistent with very fine-grained CO_2 deposits and/or optically thick clouds.

[24] The strongest spectral contrasts measured by MCS are associated with the south polar residual cap (SPRC; 30°W, 87°S), where T_{12}–T_{22} > 10 K throughout the winter, with maximum differences ~25 K. The SPRC represents the apex of a larger, spatially coherent temperature structure poleward of ~80°S with consistently low brightness temperatures and high spectral contrast. Smaller isolated low emission regions exhibit less coherence and greater time-variability, especially in the zone 70–80°S. Most of the spatial structures apparent in Figure 4 are regions of frequent low emission behavior throughout the study period, and we observe that many are at least qualitatively correlated with topographic slopes [cf. *Cornwall and Titus*, 2009, 2010]. Some regions known to exhibit high springtime albedo, notably the "Mountains of Mitchel" (320°W, 75°S) are also observed to have higher than average low-emission activity.

[25] The departure of measured south polar radiances from blackbody emission is illustrated by Figure 5. Seasonal mean spectral contrast increases nearly monotonically from 60°S toward the pole, consistent with decreasing frost grain size and/or increasing cloudiness. We calculated CO_2 frost point temperatures from latitude-binned MOLA topography with a reference pressure of 520 mb and a scale height of 7.1 km, typical of south polar winter, using CO_2 frost point data from *Brown and Ziegler* [1980]. For the measured atmospheric temperature variability in this season [*McCleese et al.*, 2008], the uncertainty in the scale height is <1 km, corresponding to a maximum uncertainty of ~0.5 K in the frost point temperature at the highest elevations. We found that 22-μm nadir brightness temperatures are substantially lower than the frost point at all latitudes within the seasonal cap, trending toward lower brightness temperatures near the pole. One possibility is that this trend is due to an actual frost point depression where the polar atmosphere is depleted in CO_2 gas relative to less volatile components such as Ar [*Kieffer et al.*, 1976]. *Sprague et al.* [2004] reported evidence for this intriguing phenomenon in the south polar winter atmosphere using the Gamma Ray Spectrometer on

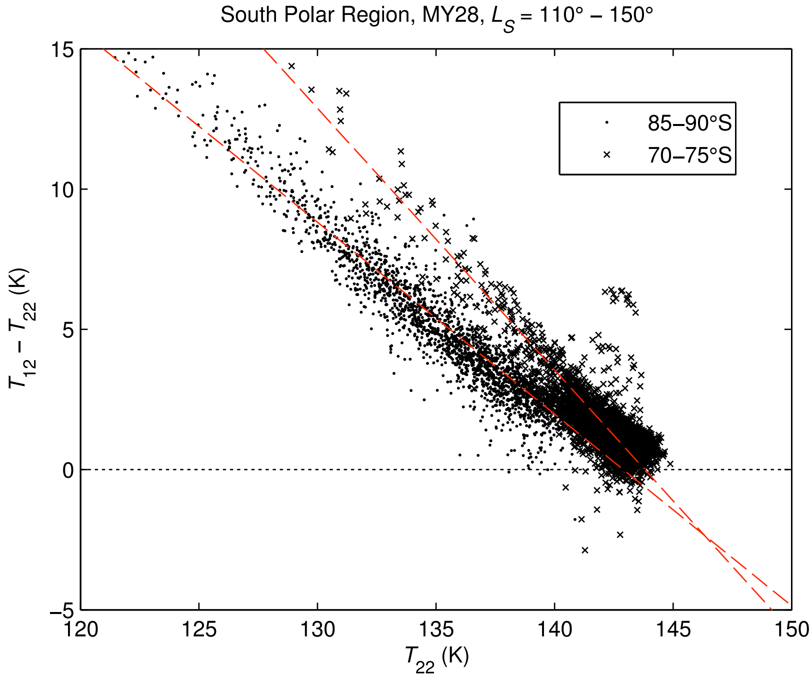

Figure 6. Spatially binned (60 × 60 km) brightness temperature data showing the strong linear correlation between the difference T_{12}–T_{22} and T_{22} in measured nadir brightness temperatures of the south seasonal ice cap. The two dashed lines are linear least squares fits to the two separate zonal bands 70–75°S and 85–90°S, excluding points with T_{12}–T_{22} < 4 K in order to capture the behavior of low emission regions only. The zeros of the linear fits indicate the approximate true surface temperature within the low emission regions, where the surface emissivity is close to blackbody behavior.

Mars Odyssey. If non-condensable gas enrichment were the only cause of low emission regions, we would measure the same brightness temperature depression in all MCS channels sensing the surface, such that T_{12}–$T_{22} \approx 0$, independent of T_{22}. In contrast, Figure 5 shows a strong correlation between these quantities, and therefore we can rule out CO_2 gas depletion as the primary cause of low emission regions, affirming the conclusion by *Hess* [1979]. In fact, the observed correlation points strongly toward infrared scattering by solid carbon dioxide, whether on the ground or in the air.

[26] In order to better characterize the infrared spectral properties of the low emission regions, we plotted spectral contrast T_{12}–T_{22} against T_{22} for each of the 60 × 60 km and 1° L_S bins (see Figure 4) throughout the south polar winter study period (Figure 6). Most of the seasonal cap exhibits T_{12}–$T_{22} \approx$ 1–2 K, indicating that regions of very strong spectral contrast do not dominate the radiative behavior of the south polar seasonal cap during this period, consistent with the snapshot in Figure 4. Those points that do exhibit strong spectral contrast show low values of 22-μm brightness temperature, defining a characteristic linear trend in the scatterplot. A similar trend was noted in the Viking IRTM nadir data [*Paige*, 1985] and is known to be indicative of fine-grained surface frosts, clouds of CO_2, or some combination of the two [*Forget et al.*, 1995]. The MCS data have spectral slopes generally consistent with previous observations, and also reveal two distinct clusters, associated with two different latitude bands. Isolating points in the band from 70° to 75°S yields the steeper slope, intersecting T_{12}–T_{22} = 0 at $T_{22} \approx$ 144 K. In the band 85° to 90°S, the slope is shallower and intersects the zero line at ~143 K. Approximately 60% of the points with T_{12}–T_{22} < 1 K also have T_{22} between these two zero-contrast temperatures. We note that these zero-contrast points define blackbody behavior, such that $T_{surface} \approx T_{22}$ and the infrared brightness temperature is inferred to be approximately equal to the thermodynamic temperature of the surface. This assumes that there is no optically thick "gray" absorber in the atmosphere, such as dust.

[27] We used MOLA topography [*Smith et al.*, 2001] along with carbon dioxide vapor pressure data [*Brown and Ziegler*, 1980] to estimate the expected frost point temperatures in the two latitude bands defined above; these are approximately 145 K and 144 K in the lower- and higher-latitude bands, respectively. We have assumed 520 Pa at zero elevation and a pressure scale height of 7.1 km, typical of the south polar winter [*Hourdin et al.*, 1993]. The difference between the expected and measured surface temperatures corresponds to a frost point reduction of ~1–2 K, or reduction in CO_2 partial pressure at the surface of ~50 Pa. A plausible explanation is depletion of gaseous CO_2 following its deposition on the surface, relative to the "non-condensable" components [*Sprague et al.*, 2004]. In this scenario, the relative non-condensable ("NC") enrichment is

$$\frac{q'_{NC}}{q_{NC}} = \frac{1 - \alpha q_{CO_2} p'_{CO_2} / p_{CO_2}}{1 - q_{CO_2}}, \quad (2)$$

where q and p are the annual average mass mixing ratios and partial pressures, and the primed quantities are their instantaneous values. The parameter α represents the ratio of total

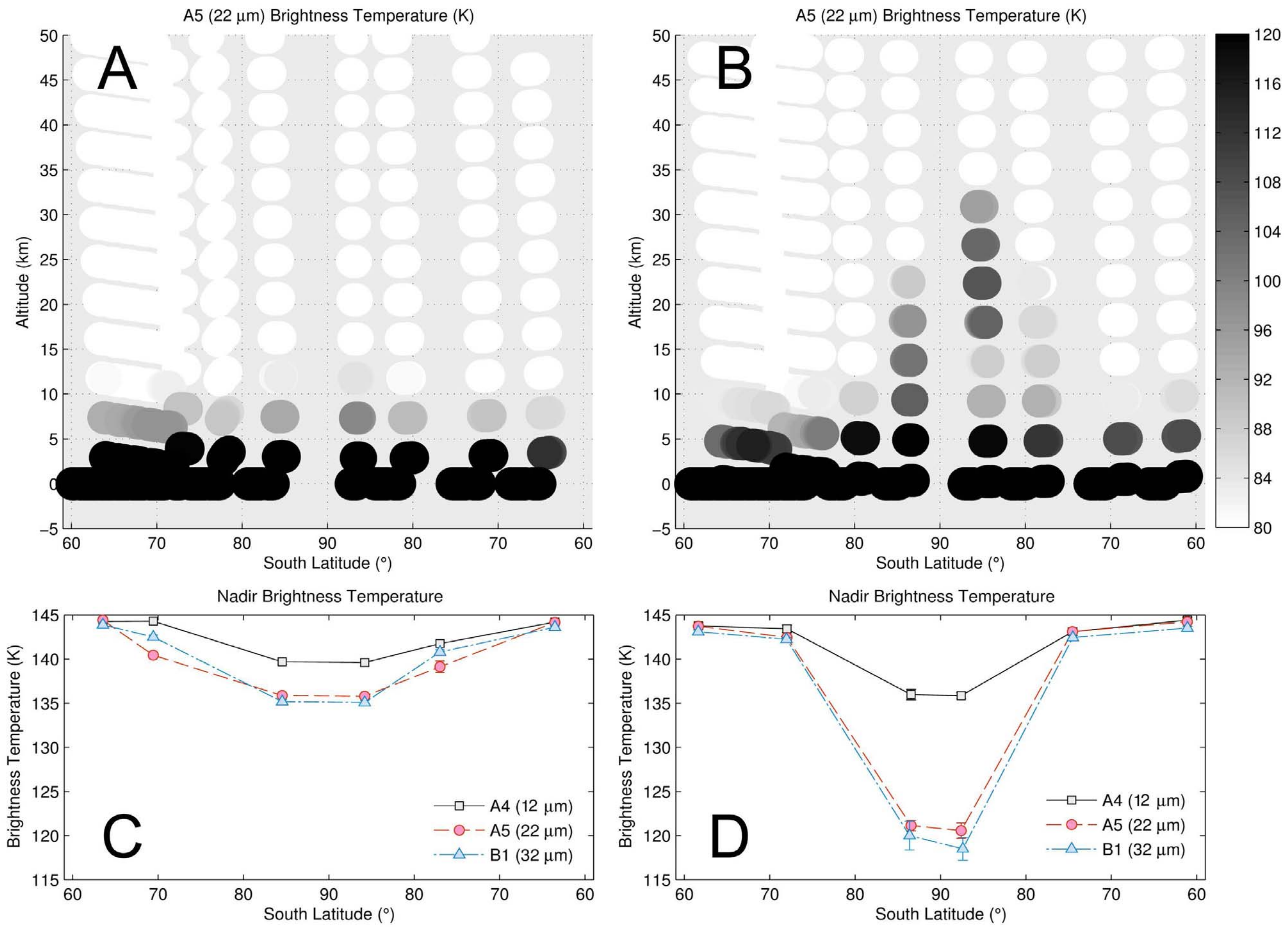

Figure 7. (a, b) Limb and (c, d) nadir transects captured by MCS for two different orbits during mid-southern winter. Limb brightness temperatures in channel A5 (22 μm) are a proxy for cloud opacity, because gases in the atmosphere are mostly transparent in this channel, and the clouds are nearly isothermal. The two orbits show distinctly different cloud activity, with a more extensive polar cloud occurring in Figure 7b. Nadir measurements taken within minutes of the limb profiles Figure 7b over the same region show strongly depressed brightness temperatures; this effect is less pronounced in Figure 7c when the clouds are commensurately thinner. Limb observations <5 km contain a significant surface contribution.

atmospheric column mass relative to the annual average; a plausible range for this season is ~0.8–0.9 [*Prettyman et al.*, 2004]. Relative to the baseline $q_{CO_2} \approx 95\%$, the empirically derived CO_2 partial pressures from MCS correspond to non-condensable gas enrichment by a factor of ~5–7 (or $q_{CO_2} \approx$ 70–80%) via equation (2), with enrichment increasing toward the pole. While other (e.g., dynamical) effects may be present, this range is generally consistent with estimates based on GRS measurements of argon during the same season [*Sprague et al.*, 2004], given the uncertainties involved. Evidence from MCS and GRS therefore suggests that wintertime depletion in CO_2 gas contributes a few degrees of real cooling to the surface inside the polar winter vortex, but is not the primary cause of the "cold spots" [cf. *Hess*, 1979; *Weiss and Ingersoll*, 2000]. For this reason, we prefer the terminology "low emission regions" to describe these anomalous infrared features.

4.2. Limb Observations

[28] Immediately after the beginning of science operations in Mars orbit, MCS detected extensive clouds in limb scans over the south pole, which was deep into its winter season ($L_S = 110°$). Cloud opacity is observed as enhanced infrared radiance in channels at wavelengths with little or no gaseous absorption (window channels) for limb tangent points near the surface up to ~50 km altitude, via both direct emission and scattering of radiation emitted by the surface below. Blanketing by clouds should reduce the infrared flux to space, which may be the cause of the low emission regions in surface-looking infrared measurements [*Kieffer*, 1979; *Paige*, 1985; *Forget et al.*, 1995]. Our goal was to quantify the correlation between the clouds and low emission regions, using the unique capability of MCS to make nearly simultaneous measurements of limb and nadir thermal emission over the poles.

[29] Qualitatively, MCS confirms that clouds are associated with low emission regions: when the polar atmosphere is cloudy, we always observe a reduction in nadir brightness temperatures, especially near 22 μm wavelength (Figure 7). Cloud opacity is variable, but generally increases toward the pole, with the most extensive and persistent cloud activity occurring over the SPRC, just where we find the lowest

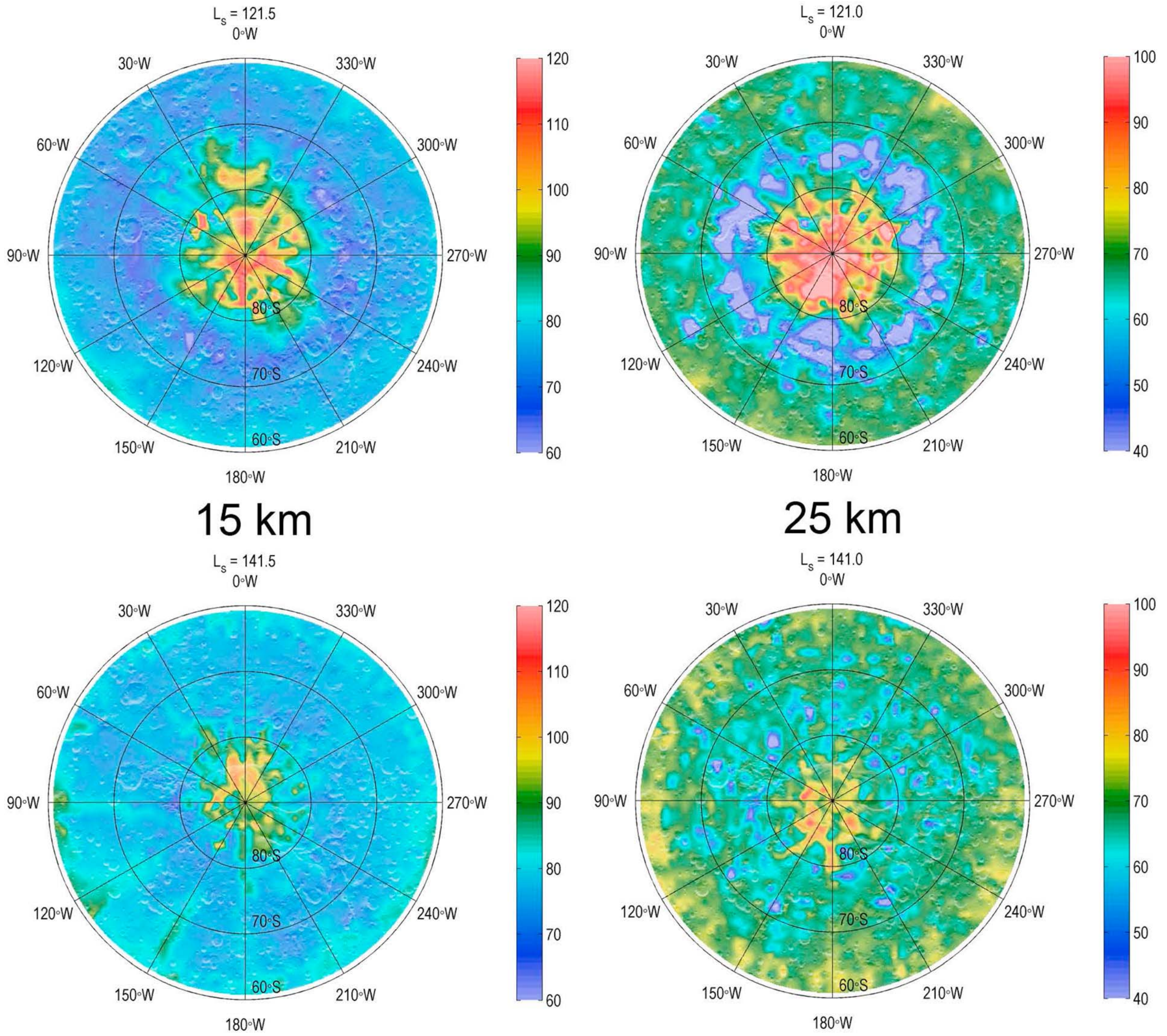

Figure 8. South polar MCS 22-μm limb tangent observations at (top) mid-winter and (bottom) late winter. The polar annulus is well-defined at midwinter within the 25-km altitude bin, and only inside 80°S do clouds extend to this altitude. Late in the winter season, the polar annulus extends to lower latitudes, but is less well defined at all altitudes, and the polar cloud begins to dissipate. The lower end of the brightness temperature scales (40–60 K) is near the noise-floor for this channel, indistinguishable from the background of space. Spatial incoherence arises from the fact that the bin size of ~60 km (chosen for consistency with nadir maps) is significantly smaller than the uncertainty in tangent point determination of ~300 km (section 2). Each panel spans a time range of 1° L_S.

nadir brightness temperatures. While most clouds appear to extend all the way to the surface, we occasionally observe detached cloud layers, most often in the altitude range ~20–30 km where *McCleese et al.* [2008] observed atmospheric temperatures closely following the CO_2 frost point. In the remainder of this section, we investigate the extent to which the CO_2 clouds (and related snowfall) cause the low emission regions.

4.2.1. Cloud Distribution and Morphology

[30] At a mid-tropospheric altitude of 15 km, clouds are thicker and more common at higher latitudes, particularly in the zone pole-ward of 80°S. An intriguing feature in the limb data is a relatively clear annulus near ~70°S, which is most pronounced in the upper troposphere in the altitude range ~20–30 km (Figure 8). By monitoring limb radiances throughout the study period, we found that, at these latitudes, transient low clouds seem to be common at low altitudes, though their presence is difficult to detect below ~5 km altitude in the limb radiances due to contamination of the signal by surface thermal emission. The clear annulus is most well-defined near mid-winter at about L_S = 120°, at which time it lies near 70°S. Later in the winter season the annulus expands, moves poleward and becomes less well-defined due to increasing water ice opacity at lower latitudes [*Benson et al.*, 2010], and decreasing polar cloud opacity; by L_S = 150° its structure is sufficiently complex that the clear region no longer resembles an annulus (Figure 8). Though detailed dynamical modeling is beyond the scope of this

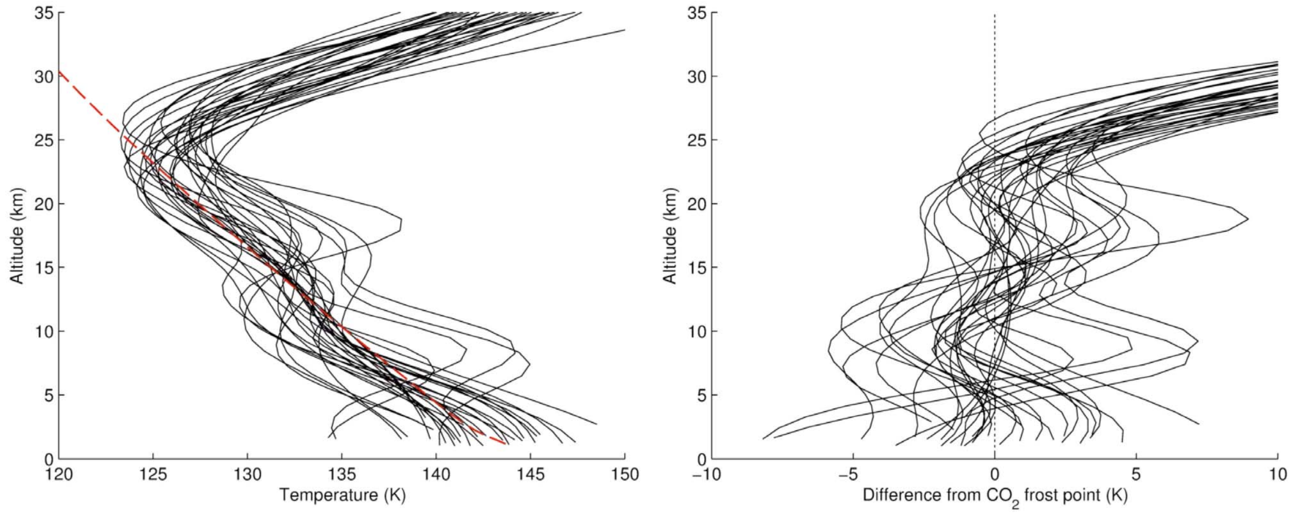

Figure 9. Temperature retrievals (solid lines) from MCS for the latitude range 85–90°S, compared to the (left) local CO_2 frost point (dashed line), and (right) difference from saturation. We note that much of the atmosphere below ~30 km is near saturation.

paper, we suggest that inhibition of poleward transport of dust and water due to the presence of a strong polar winter vortex [*McConnochie et al.*, 2003] could explain the annulus's low-latitude boundary, while the transition to persistently super-saturated air and formation of CO_2 clouds [*McCleese et al.*, 2008] could explain its higher-latitude boundary.

4.2.2. Polar Cloud Composition

[31] We examined temperature retrievals derived from MCS limb radiances, at latitudes 85–90°S during cloudy periods (Figure 9). Indeed, many of the profiles fall near (or even below) the CO_2 frost point, consistent with condensation in the lower atmosphere at altitudes where clouds have been previously observed [*Neumann et al.*, 2003]. Saturation with respect to CO_2 does not typically occur above ~30 km, consistent with the polar winter middle-atmosphere warming reported by *McCleese et al.* [2008]. Just inside the polar winter vortex, where MCS observes a consistently clear annulus (section 4.2.1), temperature profiles are typically slightly above the local CO_2 frost point. Thus, the temperature data suggest saturation within the cloudy extreme polar regions, consistent with the presence of CO_2 snow clouds.

[32] As a preliminary test of cloud composition, we isolated the spectral end-members in the MCS limb measurements where aerosol opacity is high, and applied independent component analysis (ICA) [*Hyvärinen and Oja*, 2000] to an image swath spanning the time range L_S = 110.5–111.5°, around mid-southern winter. Among the benefits of ICA is the ability to distinguish end-members based on their spectral independence and map their relative contributions to each pixel in the scene. Brightness temperatures in channels A4, A5, B1 and B2 were binned in altitude and latitude for the eastern and western hemispheres separately then stacked to form a multispectral image of the limb. Using the ICA algorithm of the IDL/ENVI™ software package (Exelis Visual Information Solutions, Boulder, Colorado) we reduced the dimensionality of the image to three spectral bands and sorted these in order of their 2-D spatial coherence. Figure 10 shows the two most spatially coherent end-members, with "end-member 1" clearly corresponding to the polar cloud. Taking the average spectra of the ~10 purest pixels for each end-member shows their distinct spectral character. Forward models for the limb spectra (see Appendix A) show that the polar cloud end-member is most consistent with CO_2 ice, while the aerosol dominating the lower latitudes ("end-member 2") is water ice. Water ice clouds are known to be common occurrences near the edges of the seasonal ice caps [*James et al.*, 1992] and were mapped in detail by *Benson et al.* [2010] using MCS opacity retrievals.

[33] While the ICA results are suggestive of CO_2 ice particles, a more robust determination requires fitting the spectral radiance profiles directly. We performed aerosol opacity retrievals on sets of 8–16 radiance profiles in the latitude range 85–90°S, on each orbit during the south polar winter study period, assuming pure compositions of CO_2 ice, water ice, and dust, each at a range of grain sizes (Figure 11). In the case of CO_2 ice, we used the B1 (32.8 μm) channel for the retrieval, based on the high extinction efficiency of CO_2 ice at this wavelength, relative to the other aerosols considered (Table 1). For water ice and dust opacity retrieval, we used channels A4 (11.9 μm) and A5 (21.9 μm) respectively, consistent with the standard MCS retrieval pipeline [*Kleinböhl et al.*, 2009]. After retrieving opacity profiles, we forward-modeled the radiance profiles in the other MCS channels not used in the retrieval, and compared these to the observations. Figure 11 shows an example for a typical cloud at L_s = 117.35°. Clearly, neither water ice nor dust with a standard grain size peak of ~1 μm can match the data in all three channels; we were also able to rule out dust and water ice with ~0.1 and 10 μm peak particle sizes based on their model misfits. Carbon dioxide ice particles ~10–100 μm result in a good fit to the data, while discrepancies become less acceptable for particle sizes <10 μm. Aerosol mixtures are also a possibility, but CO_2 ice provides the simplest match to the data.

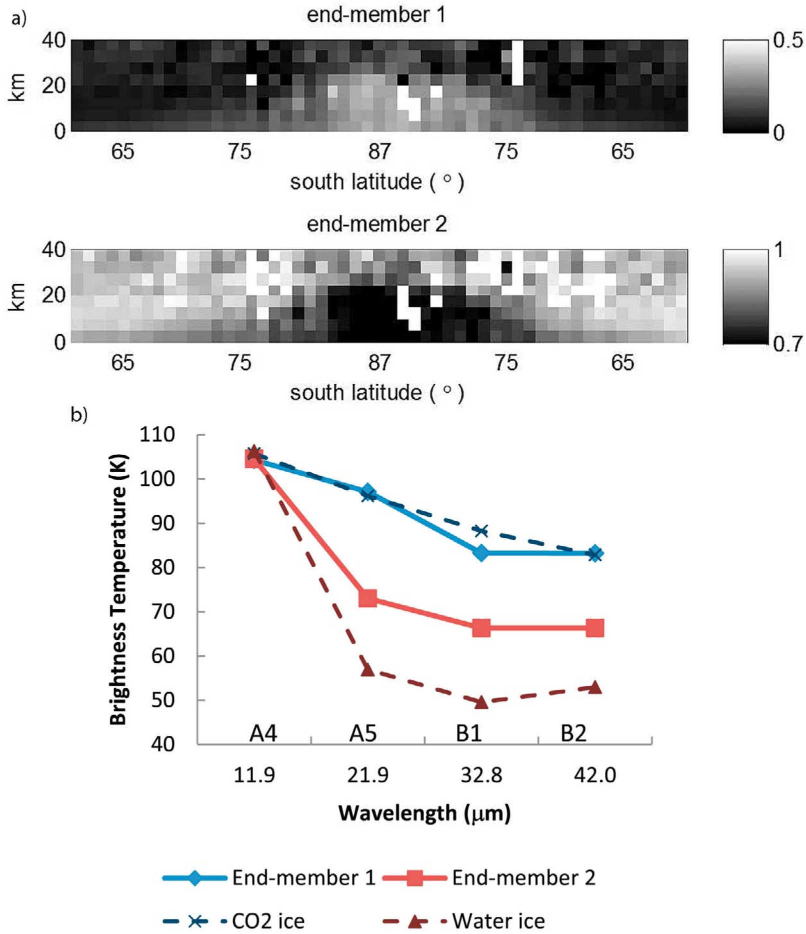

Figure 10. Spectral end-members in the south polar winter at $L_S = 111°$. (a) The mixing fraction (the relative contribution of the end-member to each pixel's spectrum) of two end-members retrieved from MCS limb data by independent component analysis (see text). (b) The extensive cloud poleward of ~70°S has a spectrum consistent with CO_2 ice, while the opacity at lower latitudes is attributed to water ice, likely with some contribution by dust. Model limb spectra (dashed curves) were calculated with the forward model using Mie parameters for carbon dioxide ice with effective radius $r_{eff} = 50$ μm and water ice with effective radius 1 μm, each with modified gamma size distribution parameters c = 10 and a = 0.1. Unit surface emissivity is assumed, with an isothermal surface and atmosphere at 145 K. Optical depth was treated as a free parameter to minimize differences in A4 brightness temperature.

4.2.3. Correlation of Clouds and Low Emission Regions

[34] We used spatially and temporally binned data to test for correlation between clouds and low emission regions. In limb measurements, clouds always appear brighter than the background of space in the 22-μm channel, so we used the brightness temperature in this channel as a proxy for cloud opacity (though other channels exhibit similar behavior). Conversely, low nadir brightness temperature in the 22-μm channel serves as a proxy for low emission regions, because this channel is near the Planck function peak for the ~145 K surface and clouds. We found good correlation between limb radiances and low emission at nadir for the 5-km altitude bin centered at 25 km, which is shown in Figure 12. In this case, the spatial bin size was increased to 300 × 300 km to improve the clarity of the plot and reduce the effects of uncertainty in limb tangent point location; this spatial scale is slightly greater than the tangent point uncertainty (section 2). The time bin size was again set to 1° of L_S. Several interesting features are immediately apparent: 1) When the atmosphere is clear ($T_{22}^{limb} < 60$ K), nadir brightness temperatures remain near 142 K, or ~2–3 K below the expected CO_2 frost point. 2) Latitudes equatorward of ~75°S (orange to red in Figure 12) show a positive correlation between nadir and limb brightness temperatures, consistent with emission by atmospheric water ice or dust particles, or a warm surface bare of seasonal ice. 3) A negative correlation exists between nadir and limb brightness temperatures for latitudes poleward of ~80°S, consistent with infrared scattering by CO_2 clouds. The fact that no data points occur in the lower left quadrant of Figure 12 implies that, at least on the 300-km and 1° of L_S scales, low emission regions did not occur under a clear sky. This does not rule out the contribution of surface deposits to low emissivity, because small-grained surface deposits can (or perhaps always do) occur concurrently with

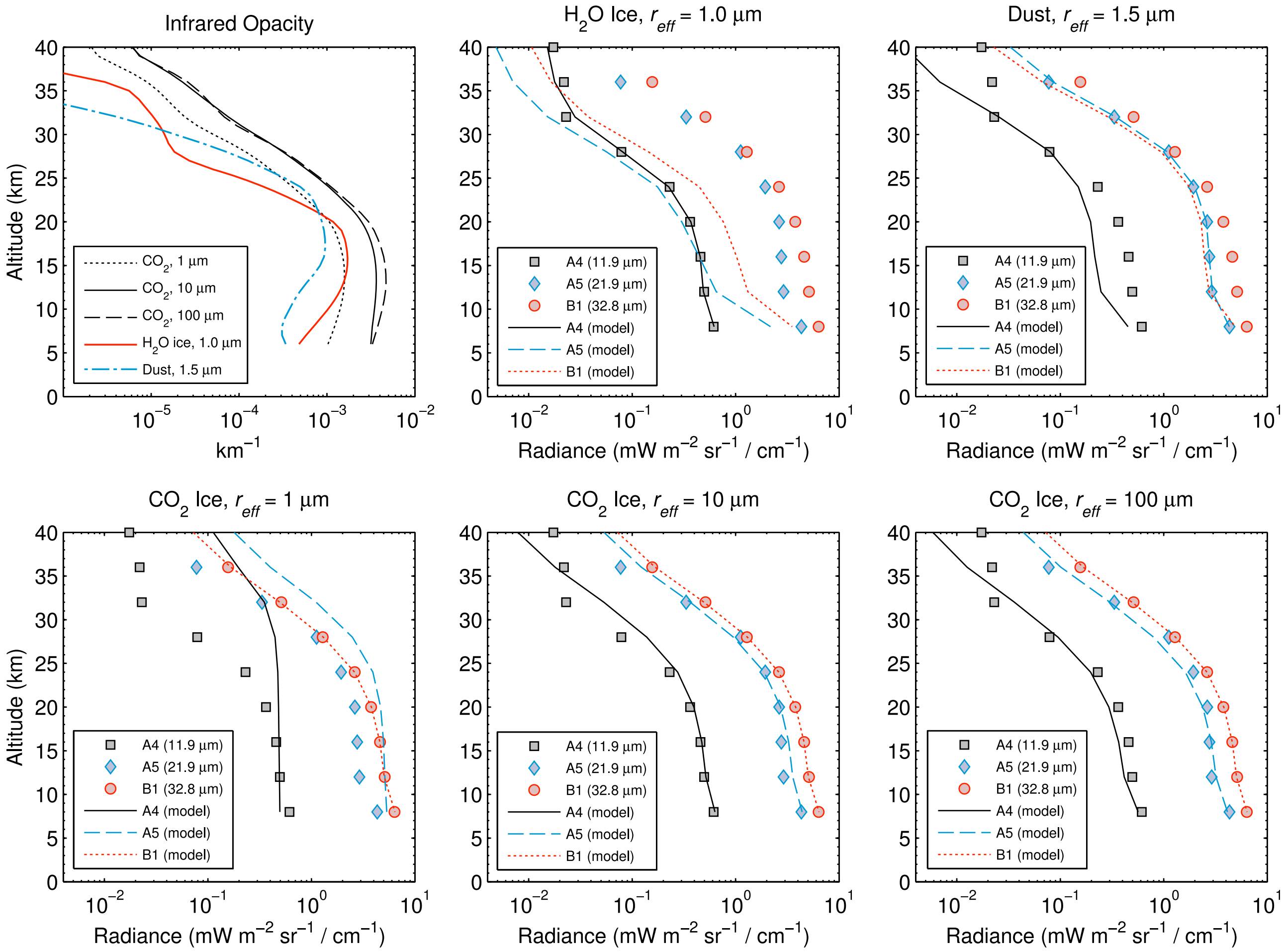

Figure 11. South polar opacity and radiance profiles based on aerosol retrievals of CO_2 ice, water ice, and dust, during MY28, L_s = 117.35°, at latitudes 85–90°S. Retrievals were performed using MCS channels A4 (water ice), A5 (dust), and B1 (CO_2 ice), and opacity is reported as extinction per kilometer in the relevant IR band.

CO_2 clouds. Also, low emission regions at scales <300 km and/or time scales shorter than a few sols, could occur independently of clouds, and be averaged out by our binning scheme. With these caveats in mind, our results indicate clouds are at least partly responsible for low emission regions.

[35] Excluding data with nadir brightness temperatures >143 K, the correlation coefficient between 22-μm brightness temperatures in the nadir and 25 km altitude for the period L_S = 110 to 150° is $R \approx -0.5$ to -0.3 (95% confidence interval). Given the large number of points ($N > 1000$), the probability that the correlation arises at random is nearly zero. Scatter in the data can be attributed to real variability in cloud particle size and optical depth, as well as variations in cloud height. It is possible that smaller clouds do not reach altitudes as high as 25 km; unfortunately, near-surface limb measurements are often contaminated by surface emission and cannot be used to establish correlation with nadir data. Nonetheless, as shown in Figure 13, the CO_2 clouds appear remarkably well correlated with average winter spectral contrast T_{12}–T_{22} at all latitudes poleward of 60°S.

[36] Small or rapidly dissipating clouds are likely to be lost in the averaging technique presented above. However, it is possible to identify some individual small-scale clouds outside the persistent polar cloud (Figure 14). Do small clouds also correlate with low nadir brightness temperatures? Their observed rapid formation and dissipation on time scales of hours or days [*Titus et al.*, 2001; *Cornwall and Titus*, 2009] makes direct correlation with nadir data difficult, since the probability of finding observations in the same spatial bin in both limb and nadir modes within this time scale is low. On the other hand, it is possible to make a phenomenological correlation. Small scale clouds (<100 km diameter) are often observed in the MCS data near topographic slopes, especially near large craters. For example, Figure 14 shows a small transient cloud observed in the vicinity of the crater Phillips, where a low emission region had also been observed within the same 1° of L_s. In fact, this particular crater is observed to be a favored location for both phenomena, though we note that temporal variations (on timescales smaller than the 1° L_s time bin) could account for the <300 km spatial structure of the kind shown in Figure 14. Thus, while a quantitative correlation is difficult to establish for low-lying or small scale clouds with the MCS data, low emission regions and low-lying clouds are observed to occur at similar locations, usually associated with topography.

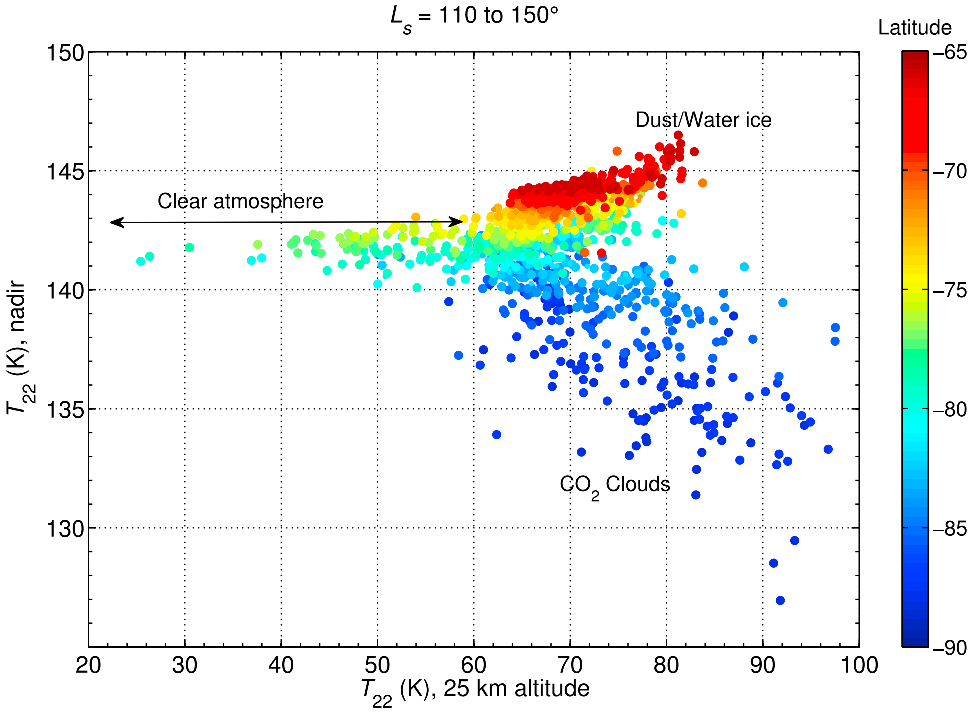

Figure 12. Scatterplot of 22-μm MCS brightness temperatures at nadir and 25 km altitude during south polar winter. Colors indicate latitude for each 300 × 300 km bin. We have made qualitative assignments to the three regions of the plot, based on the arguments in the text. The positive slope in the region labeled 'dust' may also be due to exposed ground at a temperature above the CO_2 frost point, underneath water ice clouds.

4.3. Constraints on Clouds and Frosts from MCS Nadir Observations

[37] Fitting the measured spectral contrast data provides a means of testing the range of possible frost and cloud properties consistent with the south polar winter observations. We modeled emission spectra for surface frosts (assuming infinite optical depth) of various effective grain sizes and clouds with a range of grain sizes and optical depths, attempting to minimize the discrepancy with the observed south polar cap properties (Figure 15). The results show that both clouds and frosts can independently account for the observed trend with decreasing 22-μm brightness temperature during the south polar winter study period. Pure carbon dioxide frosts have a grain size-dependent spectral contrast (smaller grains yield higher contrast) that falls on a well-defined slope closely matching the MCS nadir measurements in the latitude region 70–80°S, with a surface temperature of 144 K. However, at higher latitudes the slope

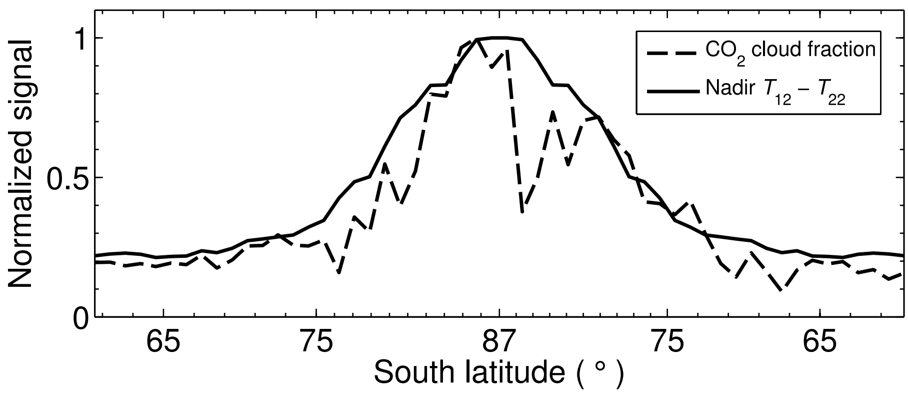

Figure 13. Altitude-averaged cloud end-member fraction and nadir spectral contrast (L_S = 111°) as a function of latitude. Cloud fraction is taken from 'end-member 1' in Figure 9, with the western hemisphere on the left and eastern hemisphere on the right, averaged from 0 to 30 km altitude. Zonal average nadir brightness temperature differences were taken directly from Figure 5, where "relative strength" indicates the ratio to the maximum difference.

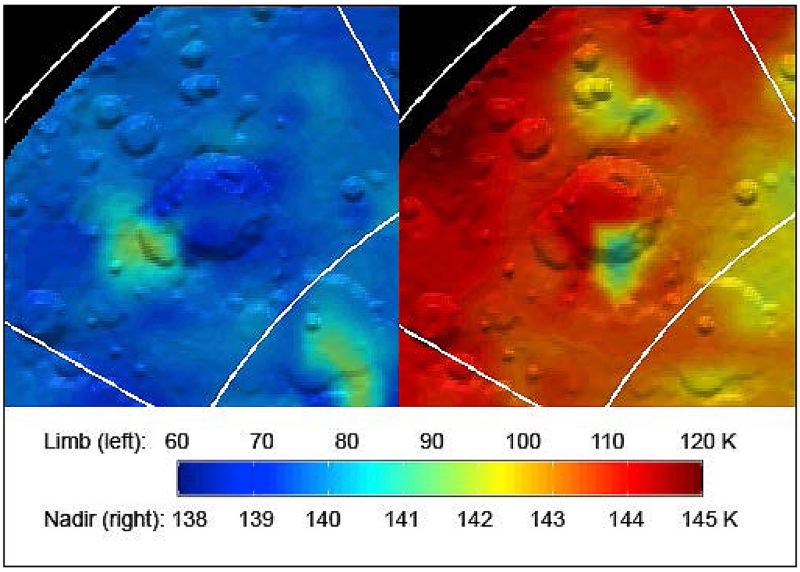

Figure 14. MCS brightness temperatures during $L_s = 120°$ (averaged over 1° L_s) reveal clouds and low nadir brightness temperatures preferentially occurring near MOLA-derived topographic slopes. The left-hand frame shows 22-μm limb data at 15 km altitude, and the right-hand frame shows 22-μm nadir data. The crater at center is Phillips (66.7°S, 305°E), where both phenomena are frequently observed, especially late in the winter season. The box width is approximately 350 km, which is somewhat larger than the limb position uncertainty of ~260 km.

is shallower, requiring the addition of some contaminant such as dust or water ice to explain the observed spectral contrast. This implies an unusual situation: if surface frosts alone are the cause of the observed low emissivities, dust or water ice content in the surface deposits must increase toward the pole, rather than decrease as expected if they are transported from lower latitudes. A reasonable alternative explanation is that cloud cover contributes significantly to the low emission regions, at least at the highest southern latitudes.

[38] As shown in Figure 15, clouds composed of pure CO_2 grains match the MCS nadir measurements just as well as surface frosts, for both zonal bands. However, in the absence

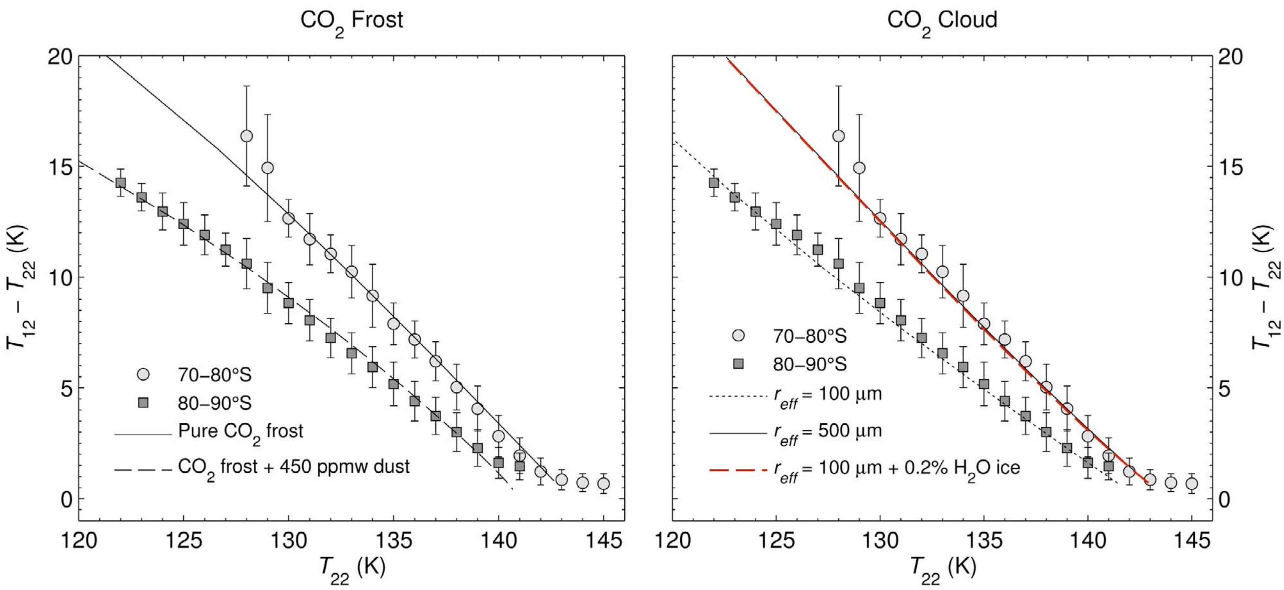

Figure 15. Wintertime nadir channel A4 and A5 spectral contrast as a function of A5 brightness temperature, separated into two latitude bands: 70–80°S, and 80–90°S, distinguished by their different slopes and intercepts in this plot. Model results for (left) granular CO_2 surface frost and (right) CO_2 ice clouds are shown for comparison. Decreasing frost grain size results in higher spectral contrast values, as does increasing cloud optical depth.

Table 2. Optical Depth Retrievals for Different MCS Channel Limb Profiles for the Polar Cloud Observed in the Single Orbit Occurring at 22:56 UTC on September 25, 2006[a]

	Total Normal Optical Depth > 4 km (Snow Particle Radius = 50 μm)				
Channel	Q_{ext}	τ_z	T_{surf}	Emissivity	τ_v (Q_v = 2.55)
4	2.25	0.19 ± 0.03	142.24	0.85	0.22 ± 0.04
5	2.38	0.19 ± 0.05	141.25	0.88	0.20 ± 0.05
7	2.39	0.14 ± 0.05	137.88	0.85	0.14 ± 0.05
8	2.51	0.14 ± 0.04	145.03	1.00	0.14 ± 0.04

[a]The latitude range of the profiles is −84.76 to −86.30°. Extinction efficiency is given in the column Q_{ext}, the infrared normal optical depth of the cloud is τ_z, surface temperature T_{surf}, and visible normal optical depth τ_v. Surface temperature (and by extension, surface emissivity) is taken as a free parameter in the retrieval. Uncertainties in the visible optical depth were estimated from the range among the retrievals used in the average.

of a strong and persistent updraft the roughly 100–500 μm grains needed to match the observed trends may not have time to form in the few tens of minutes before they settle through the thin Martian atmosphere to the ground [*Forget et al.*, 1995; *Colaprete et al.*, 2003, 2005]. While we have no robust observational constraint on grain size, coupled mesoscale and microphysical models by *Colaprete and Toon* [2002] suggest CO_2 snow storms in the lee of topographic peaks could result in average grain sizes of ~100 μm, a value consistent with steady state snow grain growth and sedimentation models by *Wood* [1999]. Nonetheless, one might question whether the ~500-μm pure CO_2 snow cloud model fit to the lower-latitude population is physically plausible given the rapid sedimentation time scale. A possible solution was offered by *Forget et al.* [1995], who showed that the addition of about 2 pr-μm of water ice (~1-μm grains) to CO_2 clouds with mode grain radii of ~50 μm could match the spectral contrast trend in the Viking-IRTM nadir data within the measurement error. We are also able to fit the MCS data with a similar mixture of water and CO_2 cloud particles, albeit for slightly larger CO_2 grains ~100 μm in radius (Figure 15). In fact, water ice particles can be identified in the limb emission spectra (cf. Figure 9), typically occurring above the CO_2 clouds. The maps of ice opacity from *Benson et al.* [2010] indicate the southern boundary of the south polar hood belt was ~65–75°S during the study period, with ice optical depths increasing toward the end of winter. Differences in the spectral slopes revealed in Figure 15 could therefore be related to differences in water ice concentrations in the two distinct zones.

4.4. Retrieval of Cloud Optical Depths From Limb Measurements

[39] The nadir observations and their correlation with the limb observations are suggestive of the role clouds play in forming low emissivity regions. Opacity profiles retrieved from MCS limb measurements can be used to directly constrain the attenuation caused by clouds. This is a nonlinear problem, which even in the simplest case requires both a forward model and knowledge of the weighting functions specifying the contribution of each altitude in the atmosphere to each measured radiance value. Iterative relaxation techniques provide an efficient, yet accurate method for obtaining solutions [e.g., *Liou*, 2002]. We applied the standard nonlinear iterative relaxation technique pioneered by *Chahine* [1968, 1970, 1972] with weighting functions proportional to the path length through each atmospheric layer, convolved to the field of view response function of the detector [*Hayne*, 2010]. Within roughly 4 km of the surface, opacity retrieval is not usually possible due to contamination of the signal by emission from the surface, and we do not use measurements within this distance of the surface as constraints on the retrieval. Surface emissivity is treated as a free parameter when on-planet measurements are available, which affects the measured infrared spectrum through both direct emission and reflection of downwelling radiation from the atmosphere. Extinction by solid CO_2 does not vary appreciably among the MCS channels (Table 2), but dust and water ice extinction efficiency are minimized relative to CO_2 ice in channel B1 (33 μm), which we therefore typically used to retrieve CO_2 ice opacity profiles. Compositional constraints (section 4.2.2) suggest nearly pure CO_2 ice particles 10–100 μm, and the persistently clear annulus 70–80°S (Figure 8) is inconsistent with meridional transport of sufficient dust from lower latitudes to account for the observed opacity near the pole. On the other hand, condensation of water vapor is possible, so we also considered clouds composed of both carbon dioxide and water ices. The retrieved optical depth is relatively insensitive to differences in assumed particle size over the range 10–100 μm, as well as mixtures with water ice. For example, we found that assuming a typical cloud is composed of 0.2% water ice particles (r_{eff} = 1.0 μm) mixed with 10-μm CO_2 particles reduces the retrieved total column optical depth by only ~15%, while significantly worsening the model fit to the observed radiance profiles, relative to assuming a pure CO_2 ice cloud (cf. Figure 11).

[40] We initially performed retrievals on an average radiance profile over the SPRC during the period L_S = 120–125°, using a coincident temperature profile retrieved from the 15-μm channels [*Kleinböhl et al.*, 2009]. During this roughly two-week period in the heart of southern winter, we find that the mean visible total normal optical depth above 5 km altitude over the SPRC is 0.19 ± 0.15 (assuming 50 μm grains), consistent with the range deduced from nadir measurements alone. If clouds are the sole cause of the high nadir spectral contrast T_{12}–T_{22} > 5 K observed during the same time interval in the nadir data, optical depths must be greater than unity (section 3.2). On the contrary, with the observed mean visible optical depth of 0.04 to 0.34, a cloud composed of 50 μm CO_2 particles will appear to have T_{12}–$T_{22} \approx 0$ to 2.5 K (Figure 3). Therefore, we conclude that on average during this period, either 1) small-grained surface frost contributes at least half the spectral contrast of the SPRC, or 2) most cloud particles lie below about 5 km altitude. We also searched for optically thick clouds too short-lived to strongly affect the average. Optical depth retrievals for a single appearance of a relatively thick polar cloud in September, 2006 are shown in Figure 16 and Table 2, as an example. Opacities are actually comparable to the seasonal mean, with the total normal visible optical depth of 0.18 (±0.05) still too small to independently explain the highest observed nadir T_{12}–T_{22}. We searched the entire southern winter MCS data set, but were unable to find individual clouds thick enough to completely explain the lowest emission regions. This indicates that either the thickest clouds have lifetimes shorter than our temporal

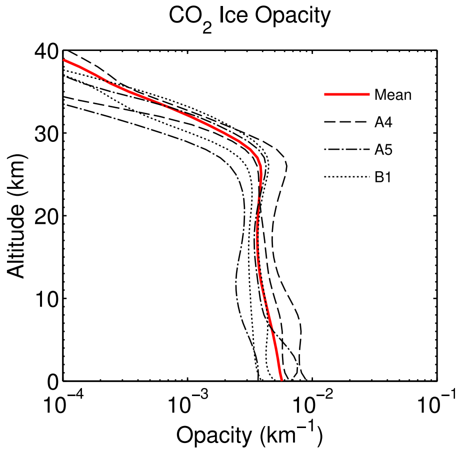

Figure 16. Carbon dioxide ice opacity retrievals for the south polar cloud occurring on the single orbit at 22:56 UTC on September 25, 2006, in the latitude range −84.76 to −86.30°. The profiles for each channel indicated in the legend correspond to the 1-sigma range in retrieved opacity, and the solid line indicates the mean profile for all channels. As in Table 2, we assumed a mode grain size of 50 μm. We adjusted the zero-level of altitude to correspond to the local surface, and detectors with altitude <5 km were not used in the retrieval. The rapid decrease in opacity above 30 km altitude is consistent with the temperature retrievals shown in Figure 9.

resolution of 1° L_S, or a substantial portion of the infrared scattering occurs below 5 km altitude, either due to low-lying clouds or surface frosts.

5. Conclusions

[41] Multispectral infrared observations by the Mars Climate Sounder reveal extensive and persistent clouds of carbon dioxide ice above the south seasonal ice cap during the polar winter of MY28. Cloud opacity increases toward the pole, with the densest and most persistent clouds occurring over the south residual cap. Nadir brightness temperatures show a similar pattern, with greater prevalence of low emission regions (aka "cold spots") poleward, and especially over the SPRC. We quantified this correlation and found that on a time scale of roughly two sols (1° L_S) and spatial scale of 300 km, low emission regions did not occur under a clear sky; conversely, where significant CO_2 clouds are observed at the limb, nadir brightness temperatures are always depressed. Together, these observations suggest that clouds are at least partly responsible for generating the low emission regions. It should be noted, however that smaller scale (and shorter-lived) low emission regions are often observed under a sky that is clear down to ~5 km altitude, although clouds may be present closer to the surface. Commonly associated with topography, these low emission regions may be generated by orographic snow clouds [cf. *Cornwall and Titus*, 2009].

[42] Because the particle sizes for pure CO_2 clouds to independently explain trends in the MCS nadir brightness temperatures (particularly in the zone 70–80°S) may be implausibly large, we conclude that either mixtures with water ice are common, or infrared scattering by surface deposits contributes a substantial fraction of the signature of low emission regions. Cloud optical depths retrieved from limb profiles are typically ~0.1 above 5 km altitude, which supports the latter case, because clouds must be optically thicker than this in order to fully explain the lowest observed brightness temperatures. Taken as an average over the southern winter study period, it appears that clouds above 5 km altitude contribute at most a few kelvins to the mean spectral contrast T_{12}–T_{22} ≈ 5 K for latitudes 80–90°S. Thus, a majority of the signal probably originates in low-lying snow clouds or small-grained surface deposits.

[43] Surface frosts, on the other hand, are not the sole cause of low emission regions either. As discussed above, the CO_2 clouds observed by MCS imply on average a few degrees Kelvin enhancement in the spectral contrast T_{12}–T_{22}, corresponding to ~5 K reduction in 22-μm brightness temperatures (Figure 1). Furthermore, models matching the MCS nadir measurements using surface frost alone require greater dust or water ice contamination at higher latitudes; this contradicts the expected trend, because these aerosols are transported from lower latitudes. We therefore conclude that low emission regions within the south polar seasonal cap are caused by the combined infrared scattering effects of granular surface deposits and coincident clouds of CO_2, with the majority of the scattering typically occurring below roughly 5 km altitude.

[44] Does it snow? Taken together, several lines of evidence indicate that CO_2 cloud particles sediment to the surface: 1) As shown throughout this paper, clouds are correlated with low emission regions, yet are too thin to fully explain the low brightness temperatures; 2) CO_2 cloud grain sizes must be >1 μm to be observed in the mid-infrared outside the 15-μm bending fundamental [*Hunt*, 1980], and will fall from one scale height (7 km) to the surface in at most a few sols, or much faster for the expected ~100 μm particles [*Forget et al.*, 1995]; 3) The clouds observed by MCS persisted in some cases for many sols, especially over the SPRC; 4) Temperature profiles retrieved by MCS during this period often show an atmosphere (super-)saturated with respect to CO_2 all the way down to the surface (Figure 9; also see *Kleinböhl et al.* [2009]). Based on these considerations, we conclude that the clouds observed by MCS are in fact carbon dioxide snow clouds, which alter the radiative balance of the seasonal polar cap both by scattering radiation directly, and creating low-emissivity snow deposits on the surface.

[45] Intriguing spatial patterns are revealed in the polar night by the MCS measurements, which may shed light on the origins and consequences of the CO_2 snow clouds. An annulus of clear air appears in the limb data by L_S = 110° and remains fairly stable at 70–80°S, especially in the altitude range 15–30 km. In this latitude band, clouds are typically short-lived and occur at low altitudes, and the air is usually slightly sub-saturated with respect to CO_2 [*McCleese et al.*, 2008]. These observations suggest an orographic origin caused by topography on the same scale as the horizontal dimension of the resulting low emission region, typically ~10 km (cf. Figures 4 and 8). At higher latitudes, a tall and persistent CO_2 cloud remains (though variable in exact location and extent) for much of southern winter, especially over the SPRC. The atmosphere here is usually saturated,

and the cloud's persistence may result simply from uninhibited radiative cooling of the atmosphere. We also showed that these two latitude bands can be separated based on their slopes in plots of nadir T_{12}–T_{22} versus T_{22}, with steeper slope in 80–90°S than 70–80°S (Figures 6 and 15). Our models suggest this difference is consistent with greater scattering by clouds on average at higher latitudes, relative to the granular surface deposits.

[46] Laser echoes from the MOLA instrument also distinguish at least two populations of clouds in the polar night, possibly representing two different grain size regimes [*Ivanov and Muhleman*, 2001; *Neumann et al.*, 2003; *Colaprete et al.*, 2003]. Over the SPRC, both types occur, whereas clouds in the lower latitude band 70–80°S are lower in altitude and dominated by returns from the MOLA channel with the shortest pulse width, possibly indicating very large grains. The lower latitude clouds were also observed by MOLA to be smaller in scale and have shorter lifetimes than the broad polar cloud associated with the SPRC. All of these observations are consistent with the MCS results, and support the conclusions above.

[47] Snowfall emerges from the observations presented in this paper as a routine occurrence during south polar winter, and a key process in determining the radiative properties of the seasonal caps. It seems that the snow clouds exert their greatest influence by depositing granular material on the surface, rather than backscattering infrared radiation themselves. As by far the snowiest place in the southern hemisphere, the south polar residual cap once again attains special status, though its low infrared emissivity is expected to reduce net deposition; perhaps this is more than counterbalanced by the high springtime albedo imparted by a long, snowy winter. Observations in the light of spring and summer by MCS and other instruments, and improved thermal models, should create the opportunity to test this hypothesis in the future.

Appendix A: An Infrared δ-Eddington Radiative Transfer Model With Arbitrary Viewing Geometry

[48] In this appendix, we describe the forward model used to simulate the combined radiative effects of clouds and surface frosts, as well as atmospheric dust and water ice. The δ-Eddington approximation [*Joseph et al.*, 1976] provides a relatively simple, yet accurate method for calculating the transfer of radiation in a scattering atmosphere. It has been successfully applied to a wide range of problems in the transfer of light through various media, from rain clouds [*Geer et al.*, 2009] to human tissue [*Cong et al.*, 2007]. The model used for the present work is based on a plane-parallel version originally developed by *Paige* [1985] for modeling infrared emission in the Mars polar regions observed by the Viking Infrared Thermal Mapper (IRTM). Three major additions or modifications were necessary in order to apply the model to the Mars Climate Sounder measurements: 1) limb viewing geometry including ray tracing along arbitrary paths through a curved atmosphere; 2) multiple cloud layers of variable aerosol composition (e.g., mixtures of water and carbon dioxide); 3) wavelength-dependent surface emissivity. These major changes necessitated re-writing the code from scratch, though the underlying algorithm is the same. We chose to write the program in the C/C++ language, following a modular programming design which is conducive to future expansion. For example, the source function can be easily changed by swapping out a single function, so that the code could be applied to the scattering of solar radiation on Mars or any other planet.

A1. The δ-Eddington Approximation

[49] In the standard Eddington approximation, the local intensity at optical depth τ is assumed to have the form

$$I(\tau, \mu) = I_0(\tau) + \mu I_1(\tau) \tag{A1}$$

where $\mu = \cos\theta$, and θ is the emission angle ($\mu > 0$ for upward radiance). For infrared wavelengths where the solar flux is small, the equation of transfer is then [cf. *Shettle and Weinman*, 1970]

$$\mu\frac{d(I_0 + \mu I_1)}{d\tau} = -(I_0 + \mu I_1) + \varpi_0(I_0 + g\mu I_1) + (1 - \varpi_0)B \tag{A2}$$

where g is the asymmetry parameter, which is the first moment of the phase function and represents the strength of forward scattering; $B = B(T, \nu)$ is the Planck radiance at the frequency ν and the local temperature T. Equation (A2) is the starting point for modeling monochromatic radiances in a layered, plane-parallel atmosphere for arbitrary temperature and aerosol profiles. With appropriate boundary conditions, the solution of (A2) for the i-th model layer is

$$I_0^i = C_1^i e^{-\kappa_i\tau_i} + C_2^i e^{+\kappa_i\tau_i} + B_i \tag{A3}$$

$$I_1^i = P_i\left(C_1^i e^{-\kappa_i\tau_i} - C_2^i e^{+\kappa_i\tau_i}\right) \tag{A4}$$

where:

$$\kappa_i = \left[3\left(1 - \varpi_0^i\right)\cdot\left(1 - \varpi_0^i g_i\right)\right]^{\frac{1}{2}} \tag{A5}$$

$$P_i = \left[3\left(1 - \varpi_0^i\right)/\left(1 - \varpi_0^i g_i\right)\right]^{\frac{1}{2}} \tag{A6}$$

τ_i is the total normal optical depth at the i-th layer, and the C_j^i are constants to be determined [*Shettle and Weinman*, 1970]. For an N-layer atmosphere, $2N$ equations are needed to determine the constants C_j^i (i = 1,2,…N; j = 0,1). Continuity between layers provides the first (2N–2) equations:

$$I_j^i(\tau_i) = I_j^{i+1}(\tau_i), i = 1, 2, \ldots, (N-1), j = 0, 1$$
$$\text{or } C_1^i e^{-\kappa_i\tau_i} + C_2^i e^{+\kappa_i\tau_i} + B_i = C_1^{i+1} e^{-\kappa_i\tau_i} + C_2^{i+1} e^{+\kappa_i\tau_i} + B_{i+1}, \text{ and} \tag{A7}$$

$$P_i\left(C_1^i e^{-\kappa_i\tau_i} - C_2^i e^{+\kappa_i\tau_i}\right) = P_{i+1}\left(C_1^{i+1} e^{-\kappa_i\tau_i} - C_2^{i+1} e^{+\kappa_i\tau_i}\right). \tag{A8}$$

The remaining two equations are provided by the diffuse irradiance conditions at the top (τ = 0) and bottom (τ = N) of the atmosphere:

$$\begin{aligned} F_{top}^{\downarrow} &= 0 = \left(1 + \tfrac{2}{3}P_1\right)C_1^1 + \left(1 - \tfrac{2}{3}P_1\right)C_2^1 + B_1 \\ F_{bot}^{\uparrow} &= \pi\varepsilon_s B_s + (1 - \varepsilon_s)F_{bot}^{\downarrow} \end{aligned} \tag{A9}$$

such that

$$C_1^N e^{-\kappa_N\tau_N}\left(1-\tfrac{2}{3}P_N\right)+C_2^N e^{+\kappa_N\tau_N}\left(1+\tfrac{2}{3}P_N\right)=\varepsilon_s(B_s-B_N)$$
$$+(1-\varepsilon_s)\left[C_1^N e^{-\kappa_N\tau_N}\left(1+\tfrac{2}{3}P_N\right)+C_2^N e^{+\kappa_N\tau_N}\left(1-\tfrac{2}{3}P_N\right)\right] \quad \text{(A10)}$$

where ε_s and B_s are the emissivity and Planck radiance of the surface, and τ_N is the optical depth of the entire atmosphere. Standard matrix methods can be used to solve this system of $2N$ equations for the constants C_j^i, which then provide a complete prescription for the intensities $I(\tau_i, \mu)$ via (A1) and (A3) through (A6). Thus, the internal radiation field of the model atmosphere (neglecting emission by gas molecules) is specified.

[50] To find the emergent intensity at the top of the atmosphere, as observed by a detector on a spacecraft, the formal solution to the equation of transfer must be integrated along the observation raypath. For on-planet observations, the integral is

$$I(0,\mu)=I(\tau_N,\mu)e^{-\tau_N/\mu}+\int_0^{\tau_N} J(t,\mu)e^{-\tau'/\mu}dt/\mu \quad \text{(A11)}$$

where, from (A2), the source function is

$$J_{Edd}(\tau,\mu)=\varpi_0(I_0+g\mu I_1)+(1-\varpi_0)B \quad \text{(A12)}$$

Whereas the standard Eddington approximation uses a scattering phase function of the form $p(\cos\Theta) = 1 + 3g(\tau)\cos\Theta$, the so-called δ-Eddington approximation [*Joseph et al.*, 1976] incorporates a δ-function to represent asymmetric scattering into the forward direction,

$$p_{\delta-Edd}(\cos\Theta)=2g^2\delta(1-\cos\Theta)+\left(1-g^2\right)(1+3g'\cos\Theta), \quad \text{(A13)}$$

which is a more realistic phase function for most aerosols of interest in planetary remote sensing. The δ-Eddington asymmetry parameter is $g' = g/(1 + g)$, where g is the standard asymmetry parameter. To use the solutions to the transfer equation derived for the Eddington approximation (A2) g is replaced by g', and the single scattering albedo ϖ_0 and optical depth τ are transformed by:

$$\tau'=\left(1-\varpi_0 g^2\right)\tau \quad \text{(A14)}$$

$$\varpi'_0=\frac{(1-g^2)\varpi_0}{1-\varpi_0 g^2} \quad \text{(A15)}$$

Using the convention $\mu' = -\mu$, so that $\mu' > 0$ for downward radiance gives the δ-Eddington transfer equation:

$$\mu'\frac{dI}{d\tau'}=I-\varpi'_0(I_0-g'\mu' I_1)-(1-\varpi'_0)B \quad \text{(A16)}$$

and a source function

$$J_{\delta-Edd}(\tau,\mu')=\varpi'_0 I_0-\varpi'_0 g'\mu' I_1+(1-\varpi'_0)B. \quad \text{(A17)}$$

A2. On-Planet Geometry

[51] In a plane parallel atmosphere (i.e.,μ = constant), for a line of sight intersecting the surface the integral term in (A11) can be calculated directly for a given source function (A17). A coordinate transformation to make downward angles positive leaves the flux boundary conditions (A10) unchanged, so that using (A3) and (A4), inserting (A1) into the integral equation (A11) gives

$$I(0,\mu')=e^{-\tau_z(N)/\mu'}\left\{(1-\varepsilon_s)\left[C_1^N e^{-\kappa\tau_z(N)}\left(1+\frac{2}{3}P_N\right)+C_2^N e^{+\kappa\tau_z(N)}\left(1-\frac{2}{3}P_N\right)+B_N\right]+\varepsilon_s B_s\right\}$$
$$+\int_0^{\tau_N}\left\{\frac{\varpi'_0}{\mu'}C_1 e^{\left(-\kappa-\frac{1}{\mu'}\right)t}[1-g'\mu' P]+\frac{\varpi'}{\mu'}C_2 e^{\left(+\kappa-\frac{1}{\mu'}\right)t}[1+g'\mu' P]+\frac{B}{\mu'}e^{-t/\mu'}\right\}dt \quad \text{(A18)}$$

where the emission angle μ' is constant for a plane-parallel atmosphere. The integral term has the solution

$$D_i=\frac{\varpi'^i_0}{-\mu'\kappa_i-1}C_1^i e^{\left(-\kappa_i-\frac{1}{\mu'}\right)\tau_i}[1-g'_i\mu' P_i]+\frac{\varpi'^i_0}{\mu'\kappa_i-1}C_2^i e^{\left(+\kappa_i-\frac{1}{\mu'}\right)\tau_i}[1+g'_i\mu' P_i]-B_i e^{-\tau_i/\mu'} \quad \text{(A19)}$$

where the coefficients are evaluated at the given optical depth τ_i. For an N-layer atmosphere, (A18) is integrated by approximating the integral as the sum of differences in (A19) between layers:

$$I(0,\mu')=e^{-\tau_N/\mu'}\left\{(1-\varepsilon_s)\left[C_1^N e^{-\kappa\tau_N}\left(1-\frac{2}{3}P_N\right)+C_2^N e^{+\kappa\tau_N}\left(1+\frac{2}{3}P_N\right)+B_N\right]+\varepsilon_s B_s\right\}+\sum_{i=1}^{N}D_i(\tau_{i+1})-D_i(\tau_i) \quad \text{(A20)}$$

Given an appropriate set of optical parameters, the extremely efficient δ-Eddington method provides accurate radiances within $\sim$1% of the exact solution for a range of optical depths and emission angles [*Joseph et al.*, 1976].

A3. Limb Viewing Geometry

[52] *Chandrasekhar* [1960] presented the formal radiative transfer solution for a problem with spherical symmetry, which in principle can be solved analytically for certain aerosol distributions. However, for an arbitrary opacity profile, the equation of transfer must be integrated numerically. For a line of sight not intersecting a surface, (A11) takes the form

$$I(s)=\int_{s_0}^{s} J(s')e^{-\beta(s',s)}\alpha(s')ds' \quad \text{(A21)}$$

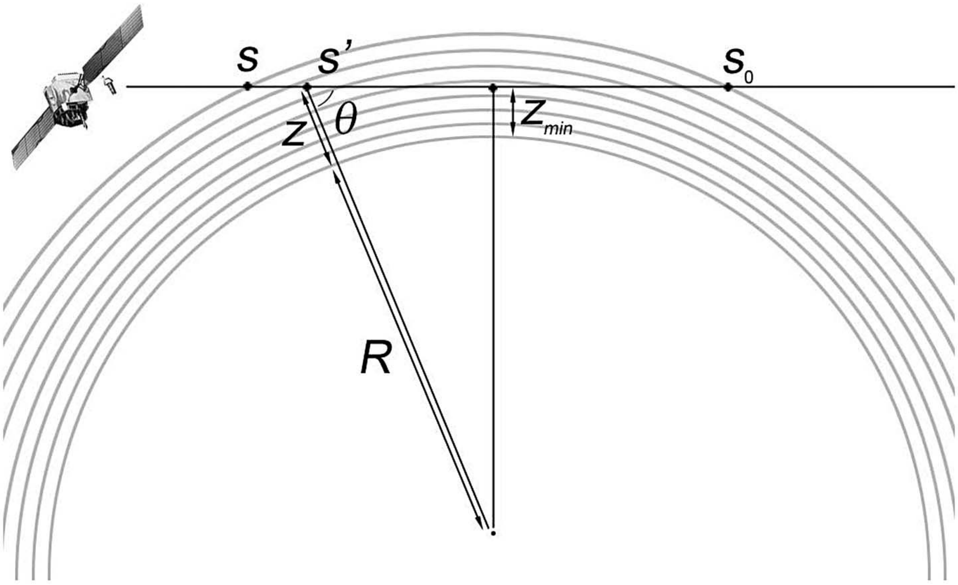

Figure A1. Limb viewing geometry for a multilayer atmosphere. Geometric quantities are labeled with reference to equation (16). The total radiance received at the sensor is given by integrating the source function along the line of sight from s_0 to s, where the distance s' at an altitude z is given by $(R + z)\cos\theta$.

where J is the source function (A17), $\alpha = k\rho$ is the opacity (per unit distance), s is distance from the sensor to the top of the atmosphere along the line of sight, and s_0 is the distance to the opposite boundary, typically the top of the atmosphere at the far limb. The function $\beta(s_1, s_2) = \int_{s_1}^{s_2} \alpha(s)ds$ gives the total optical depth between two points along the raypath. The viewing geometry is illustrated in Figure A1. Inserting the source function (A17) into (A21) yields

$$I(s) = \int_s^{s_0} \left[\varpi'_0 C_1 e^{-\kappa\tau_z}(1 - g'\mu'P) + \varpi'_0 C_2 e^{+\kappa\tau_z}(1 + g'\mu'P) + B\right] e^{-\beta}\alpha ds. \tag{A22}$$

Since the total optical depth β is itself an integral function that depends on the opacity profile and the viewing geometry, an analytical solution to (A22) cannot be determined a priori, so numerical integration is necessary. For an N-layer atmosphere,

$$\alpha ds = (k\rho)ds = -\left(\frac{d\tau_z}{dz}\right)ds, \tag{A23}$$

$$\beta_i = \int_{s_{top}}^{s_i} \alpha ds \approx \sum_{j=1}^{j=i} \Delta\tau_z^j/\mu'_j = \sum_{j=1}^{j=i} \Delta\tau_j, \tag{A24}$$

where $\Delta\tau_z^j$ is the normal optical thickness of layer j (with j = 1 the topmost layer), $\Delta\tau_j$ is the layer's line-of-sight optical thickness, and again $\mu' > 0$ downward. For a ray with a tangent point in layer j, the emergent intensity (A22) is then approximately

$$I_j = \int_0^{s_j} J(-\mu')e^{-\beta(s)}\alpha ds + \int_{s_j}^{0} J(+\mu')e^{-(2\beta(s_j)-\beta(s))}\alpha ds \quad (0 \le \mu' \le 1)$$
$$\approx \sum_{i=1}^{j} J_i(-\mu'_i)e^{-\beta_i}\Delta\tau_i + \sum_{i=j-1}^{i=1} J_i(+\mu'_i)e^{-(2\beta_j-\beta_i)}\Delta\tau_i \tag{A25}$$

where $J(\tau_z, \mu', g', C_1, C_2, \ldots)$ is the source function (in brackets in (A22)), and each of the layer-specific parameters is evaluated at the current layer. The first term in (A25) represents the integration upward ($\mu' < 0$) from the lowest layer intersected by the chord, up to the top of the atmosphere. The second term in (A25) is the integral through the same layers, but this time downward ($\mu' > 0$) from the top of the atmosphere along the farther half of the chord.

A4. Model Validation and Error Estimation

[53] A plane-parallel version of the δ-Eddington model described in this appendix has been tested extensively against more exact models validated for Mars polar winter conditions [*Paige*, 1985]. The full spherical-geometry version of the model was also extensively tested against models developed by the Mars Climate Sounder team for retrieval of water ice and dust opacity [*Kleinböhl et al.*, 2011; *Benson et al.*, 2010; *Heavens et al.*, 2011], and more rigorous multiple-scattering codes [*Irwin et al.*, 2008]. In Figure A2, we present two of these test cases: 1) a midlatitude summer temperature profile and homogeneous dust loading and a total normal optical depth of 0.027 in the A5 (22 μm) channel (case 'T1 + D1'), and 2) a polar winter temperature

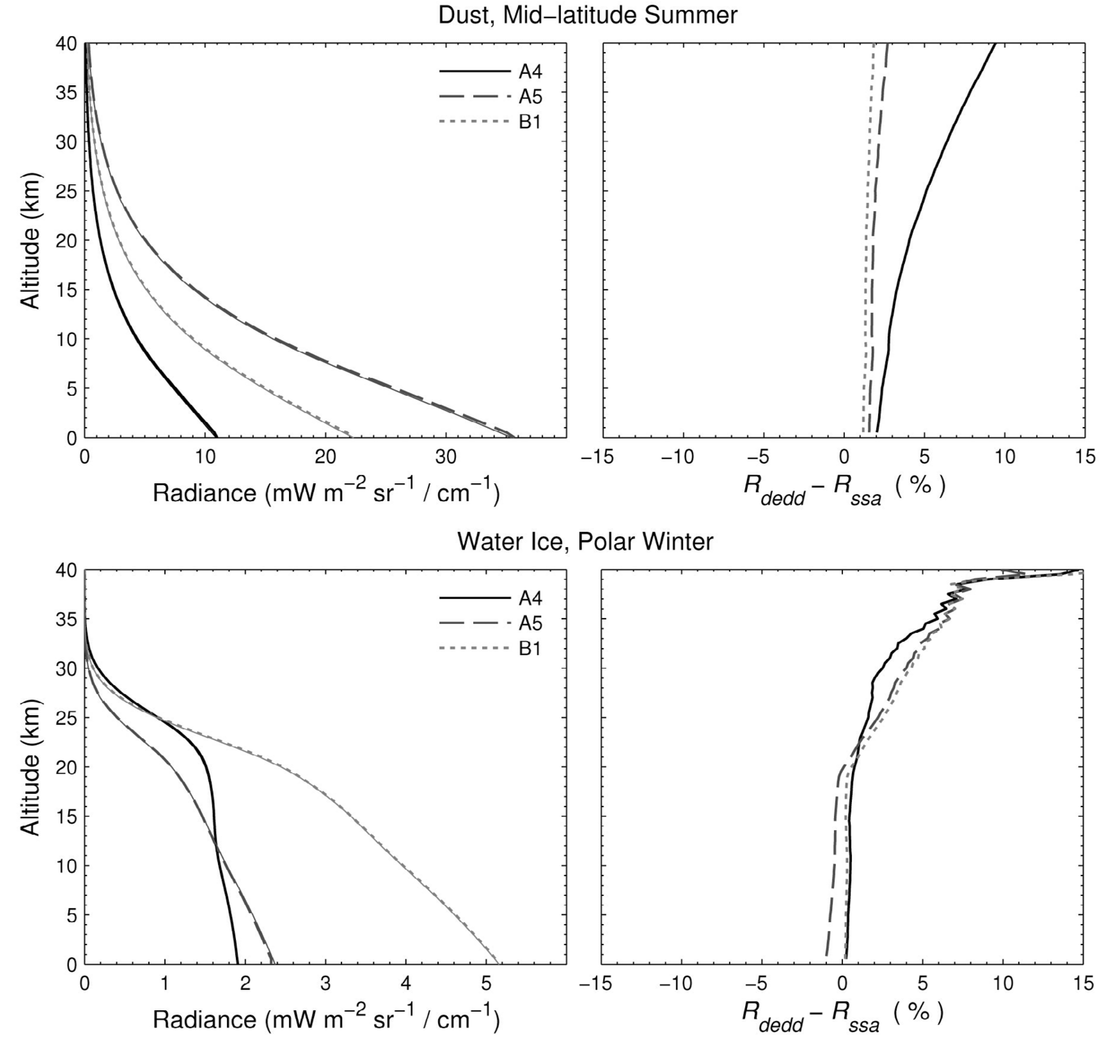

Figure A2. Comparisons between the δ-Eddington ('dedd', thick lines in Figure A2, left) model presented in Appendix A, and the single-scattering model ('ssa', thin solid lines) of *Kleinböhl et al.* [2011]. (left) The modeled radiances and (right) the relative differences (percent) between the two models for the (top) 'T1 + D1' case and (bottom) 'T2 + H4' case, as described in the text.

profile with constant water ice opacity below 20 km (rapidly decreasing to zero at higher altitudes), with total A4 (12 μm) optical depth of 0.10 (case 'T2 + H4'). Discrepancies between the δ-Eddington model and the single-scattering model are quite small at all altitudes, well within the variance among the ~4–10 radiance profiles typically averaged before performing each opacity retrieval. Typical errors in total normal optical depth associated with this spatial and temporal averaging are estimated to be ~0.01–0.1, depending on the channel and homogeneity of the cloud (see Table 2).

[54] **Acknowledgments.** We thank Oded Aharonson, James H. Shirley, and Jennifer L. Benson for useful discussions and advice during the preparation of this manuscript. P.O.H. wishes to acknowledge the invaluable support and criticism of the members of his dissertation committee at UCLA: David A. Paige, Gerald Schubert, K. N. Liou, and Christopher Russell. Part of this research was carried out at the Jet Propulsion Laboratory, California Institute of Technology, under a contract with the National Aeronautics and Space Administration.

References

Benson, J. L., D. M. Kass, A. Kleinböhl, D. J. McCleese, J. T. Schofield, and F. W. Taylor (2010), Mars' south polar hood as observed by the Mars Climate Sounder, *J. Geophys. Res.*, *115*, E12015, doi:10.1029/2009JE003554.

Brown, G. N., and W. T. Ziegler (1980), Vapor pressure and heats of vaporization and sublimation of liquids and solids of interest in cryogenics below 1–atm pressure, *Adv. Cryogenic Eng.*, *25*, 662–670.

Chahine, M. T. (1968), Determination of the temperature profile in an atmosphere from its outgoing radiance, *J. Opt. Soc. Am.*, *58*, 1634, doi:10.1364/JOSA.58.001634.

Chahine, M. T. (1970), Inverse problems in radiative transfer: Determination of atmospheric parameters, *J. Atmos. Sci.*, *27*, 960, doi:10.1175/1520-0469(1970)027<0960:IPIRTD>2.0.CO;2.

Chahine, M. T. (1972), A general relaxation method for inverse solution of the full radiative transfer equation, *J. Atmos. Sci.*, *29*, 741–747, doi:10.1175/1520-0469(1972)029<0741:AGRMFI>2.0.CO;2.

Chandrasekhar, S. (1960), *Radiative Transfer*, Dover, New York.

Clancy, R. T., B. J. Sandor, M. J. Wolff, P. R. Christensen, M. D. Smith, J. C. Pearl, B. J. Conrath, and R. J. Wilson (2000), An intercomparison of ground-based millimeter, MGS TES, and Viking atmospheric temperature measurements: Seasonal and interannual variability of temperatures and dust loading in the global Mars atmosphere, *J. Geophys. Res.*, *105*(E4), 9553–9571, doi:10.1029/1999JE001089.

Clark, R. N. (1999), Spectroscopy of rocks and minerals and principles of spectroscopy, in *Manual of Remote Sensing*, vol. 3, *Remote Sensing for the Earth Sciences*, edited by A. N. Rencz, pp. 3–58, John Wiley, New York.
Clark, R. N., F. P. Fanale, and A. P. Zent (1983), Frost grain size metamorphism - Implications for remote sensing of planetary surfaces, *Icarus*, *56*, 233–245, doi:10.1016/0019-1035(83)90036-2.
Colaprete, A., and O. B. Toon (2002), Carbon dioxide snow storms during the polar night on Mars, *J. Geophys. Res.*, *107*(E7), 5051, doi:10.1029/2001JE001758.
Colaprete, A., R. M. Haberle, and O. B. Toon (2003), Formation of convective carbon dioxide clouds near the south pole of Mars, *J. Geophys. Res.*, *108*(E7), 5081, doi:10.1029/2003JE002053.
Colaprete, A., J. R. Barnes, R. M. Haberle, J. L. Hollingsworth, H. H. Kieffer, and T. N. Titus (2005), Albedo of the south pole on Mars determined by topographic forcing of atmosphere dynamics, *Nature*, *435*, 184–188, doi:10.1038/nature03561.
Cong, W., H. Shen, A. Cong, Y. Wang, and G. Wang (2007), Modeling photon propagation in biological tissues using a generalized Delta-Eddington phase function, *Phys. Rev. E*, *76*(5), 051913, doi:10.1103/PhysRevE.76.051913.
Cornwall, C., and T. N. Titus (2009), Spatial and temporal distributions of Martian north polar cold spots before, during, and after the global dust storm of 2001, *J. Geophys. Res.*, *114*, E02003, doi:10.1029/2008JE003243.
Cornwall, C., and T. N. Titus (2010), A comparison of Martian north and south polar cold spots and the long-term effects of the 2001 global dust storm, *J. Geophys. Res.*, *115*, E06011, doi:10.1029/2009JE003514.
Deirmendjian, D. (1969), *Electromagnetic Scattering on Spherical Polydispersions*, pp. 75–119, Elsevier, New York.
Ditteon, R., and H. H. Kieffer (1979), Optical properties of solid CO_2: Application to Mars, *J. Geophys. Res.*, *84*(B14), 8294–8300, doi:10.1029/JB084iB14p08294.
Eluszkiewicz, J. (1993), On the microphysical state of the Martian seasonal caps, *Icarus*, *103*, 43–48, doi:10.1006/icar.1993.1056.
Eluszkiewicz, J., et al. (2005), A microphysically based approach to modeling emissivity and albedo of the Martian seasonal caps, *Icarus*, *174*, 524–534, doi:10.1016/j.icarus.2004.05.025.
Forget, F., G. B. Hansen, and J. B. Pollack (1995), Low brightness temperatures of Martian polar caps: CO2 clouds or low surface emissivity?, *J. Geophys. Res.*, *100*(E10), 21,219–21,234, doi:10.1029/95JE02378.
Forget, F., F. Hourdin, and O. Talagrand (1998), CO_2 Snowfall on Mars: Simulation with a general circulation model, *Icarus*, *131*, 302–316, doi:10.1006/icar.1997.5874.
Geer, A. J., P. Bauer, and C. W. O'Dell (2009), A revised cloud overlap scheme for fast microwave radiative transfer in rain and cloud, *J. Appl. Meteorol. Climatol.*, *48*, 2257–2270, doi:10.1175/2009JAMC2170.1.
Gierasch, P. J., and R. M. Goody (1968), A study of the thermal and dynamical structure of the Martian lower atmosphere, *Planet. Space Sci.*, *16*, 615, doi:10.1016/0032-0633(68)90102-5.
Hansen, G. B. (1997), The infrared absorption spectrum of carbon dioxide ice from 1.8 to 333 μm, *J. Geophys. Res.*, *102*(E9), 21,569–21,587, doi:10.1029/97JE01875.
Hansen, G. B. (1999), Control of the radiative behavior of the Martian polar caps by surface CO_2 ice: Evidence from Mars Global Surveyor measurements, *J. Geophys. Res.*, *104*(E7), 16,471–16,486, doi:10.1029/1998JE000626.
Hansen, J. E., and L. D. Travis (1974), Light scattering in planetary atmospheres, *Space Sci. Rev.*, *16*, 527–610, doi:10.1007/BF00168069.
Hapke, B. (1993), *Topics in Remote Sensing*, vol. 3, *Theory of Reflectance and Emittance Spectroscopy*, Cambridge Univ. Press, Cambridge, U. K., doi:10.1017/CBO9780511524998.
Hayne, P. O. (2010), Snow clouds on Mars and ice on the Moon, PhD thesis, Dept. of Earth and Space Sci., Univ. of Calif., Los Angeles.
Heavens, N. G., M. I. Richardson, A. Kleinböhl, D. M. Kass, D. J. McCleese, W. Abdou, J. L. Benson, J. T. Schofield, J. H. Shirley, and P. M. Wolkenberg (2011), The vertical distribution of dust in the Martian atmosphere during northern spring and summer: Observations by the Mars Climate Sounder and analysis of zonal average vertical dust profiles, *J. Geophys. Res.*, *116*, E04003, doi:10.1029/2010JE003691.
Henderson, V. and E. Sayfi (2007), Mars Climate Sounder reduced data record software interface specification, *NASA Planet. Data Syst.*, *D-37297*, NASA, Washington, D. C.
Hess, S. L. (1979), Static stability and thermal wind in an atmosphere of variable composition: Applications to Mars, *J. Geophys. Res.*, *84*(B6), 2969–2973, doi:10.1029/JB084iB06p02969.
Hourdin, F., et al. (1993), Meteorological variability and the annual surface pressure cycle on Mars, *J. Atmos. Sci.*, *50*(21), 3625–3640, doi:10.1175/1520-0469(1993)050<3625:MVATAS>2.0.CO;2.
Hunt, G. E. (1980), On the infrared radiative properties of CO_2 ice clouds: Application to Mars, *Geophys. Res. Lett.*, *7*(7), 481–484, doi:10.1029/GL007i007p00481.
Hyvärinen, A., and E. Oja (2000), Independent component analysis: Algorithms and applications, *Neural Netw.*, *13*, 411–430, doi:10.1016/S0893-6080(00)00026-5.
Irwin, P. G. J., et al. (2008), The NEMESIS planetary atmosphere radiative transfer and retrieval tool, *J. Quant. Spectrosc. Radiat. Transf.*, *109*(6), 1136–1150, doi:10.1016/j.jqsrt.2007.11.006.
Ivanov, A. B., and D. O. Muhleman (2001), Cloud reflection observations: Results from the Mars Orbiter Laser Altimeter, *Icarus*, *154*, 190–206, doi:10.1006/icar.2001.6686.
Jakosky, B. M. and Haberle, R. M. (1990), Year-to-year instability of the Mars south polar cap, *J. Geophys. Res.*, *95*(B2), 1359–1365. doi:10.1029/JB095iB02p01359.
James, P. B., H. H. Kieffer, and D. A. Paige (1992), The seasonal cycle of carbon dioxide on Mars, in *Mars*, edited by H. H. Kieffer et al., pp. 1–33, Univ. of Ariz. Press, Tucson.
Joseph, J. H., W. J. Wiscombe, and J. A. Weinman (1976), The delta-Eddington approximation for radiative flux transfer, *J. Atmos. Sci.*, *33*, 2452–2459, doi:10.1175/1520-0469(1976)033<2452:TDEAFR>2.0.CO;2.
Kieffer, H. H. (1979), Mars south polar spring and summer temperatures: A residual CO_2 frost, *J. Geophys. Res.*, *84*(B14), 8263–8288, doi:10.1029/JB084iB14p08263.
Kieffer, H. H., S. C. Chase, E. D. Miner, F. D. Palluconi, G. Münch, G. Neugebauer, and T. Z. Martin (1976), Infrared thermal mapping of the Martian surface and atmosphere: First results, *Science*, *193*, 780–786, doi:10.1126/science.193.4255.780.
Kieffer, H. H., T. Z. Martin, A. R. Peterfreund, B. M. Jakosky, E. D. Miner, and F. D. Palluconi (1977), Thermal and albedo mapping of Mars during the Viking primary mission, *J. Geophys. Res.*, *82*(28), 4249–4291, doi:10.1029/JS082i028p04249.
Kieffer, H. H., T. N. Titus, K. F. Mullins, and P. R. Christensen (2000), Mars south polar spring and summer behavior observed by TES: Seasonal cap evolution controlled by frost grain size, *J. Geophys. Res.*, *105* (E4), 9653–9699, doi:10.1029/1999JE001136.
Kleinböhl, A., et al. (2009), Mars Climate Sounder limb profile retrieval of atmospheric temperature, pressure, and dust and water ice opacity, *J. Geophys. Res.*, *114*, E10006, doi:10.1029/2009JE003358.
Kleinböhl, A., J. T. Schofield, W. A. Abdou, P. G. Irwin, and R. J. de Kok (2011), A single-scattering approximation for infrared radiative transfer in limb geometry in the Martian atmosphere, *J. Quant. Spectrosc. Radiat. Transfer*, *112*, 1568–1580, doi:10.1016/j.jqsrt.2011.03.006.
Langevin, Y. et al. (2006), No signature of clear CO_2 ice from the 'cryptic' regions in Mars' south seasonal polar cap, *Nature*, *442*, 790–792, doi:10.1038/nature05012.
Leighton, R. B., and B. C. Murray (1966), Behavior of carbon dioxide and other volatiles on Mars, *Science*, *153*, 136–144, doi:10.1126/science.153.3732.136.
Liou, K. N. (2002), *An Introduction to Atmospheric Radiation*, 2nd ed., Academic, San Diego, Calif.
McCleese, D. J., J. T. Schofield, F. W. Taylor, S. B. Calcutt, M. C. Foote, D. M. Kass, C. B. Leovy, D. A. Paige, P. L. Read, and R. W. Zurek (2007), Mars Climate Sounder: An investigation of thermal and water vapor structure, dust and condensate distributions in the atmosphere, and energy balance of the polar regions, *J. Geophys. Res.*, *112*, E05S06, doi:10.1029/2006JE002790.
McCleese, D. J., et al. (2008), Intense polar temperature inversion in the middle atmosphere on Mars, *Nat. Geosci.*, *1*, 745–749, doi:10.1038/ngeo332.
McConnochie, T. H., B. J. Conrath, P. J. Gierasch, D. Banfield, and M. D. Smith (2003), Observations of the Mars Polar Vortex, in *Sixth International Conference on Mars, Pasadena CA [CD-ROM]*, *LPI Contrib.*, *1164*, Abstract 3248.
Neumann, G. A., D. E. Smith, and M. T. Zuber (2003), Two Mars years of clouds detected by the Mars Orbiter Laser Altimeter, *J. Geophys. Res.*, *108*(E4), 5023, doi:10.1029/2002JE001849.
Paige, D. A. (1985), The annual heat balance of the Martian polar caps from Viking observations, PhD thesis, Div. of Geol. and Planet. Sci., Calif. Inst. of Tech., Pasadena.
Paige, D. A., and A. P. Ingersoll (1985), Annual heat balance of Martian polar caps: Viking observations, *Science*, *228*, 1160–1168, doi:10.1126/science.228.4704.1160.
Prettyman, T. H. et al. (2004), Seasonal cycle of carbon dioxide and atmospheric circulation in Mars' southern hemisphere as observed by neutron spectroscopy, *Lunar Planet. Sci.*, *XXXV*, Abstract 1878.
Shettle, E. P., and J. A. Weinman (1970), The transfer of solar irradiance through inhomogeneous turbid atmospheres evaluated by Eddington's

approximation, *J. Atmos. Sci.*, *27*, 1048–1055, doi:10.1175/1520-0469(1970)027<1048:TTOSIT>2.0.CO;2.

Smith, D. E., M. T. Zuber, and G. A. Neumann (2001), Seasonal variations of snow depth on Mars, *Science*, *294*, 2141–2146, doi:10.1126/science.1066556.

Sprague, A. L., W. V. Boynton, K. E. Kerry, D. M. Janes, D. M. Hunten, K. J. Kim, R. C. Reedy, and A. E. Metzger (2004), Mars' south polar Ar enhancement: A tracer for south polar seasonal meridional mixing, *Science*, *306*, 1364–1367, doi:10.1126/science.1098496.

Titus, T. N., H. H. Kieffer, K. F. Mullins, and P. R. Christensen (2001), TES premapping data: Slab ice and snow flurries in the Martian north polar night, *J. Geophys. Res.*, *106*(E10), 23,181–23,196, doi:10.1029/2000JE001284.

Warren, S. G., and R. E. Brandt (2008), Optical constants of ice from the ultraviolet to the microwave: A revised compilation, *J. Geophys. Res.*, *113*, D14220, doi:10.1029/2007JD009744.

Weiss, B. P., and A. P. Ingersoll (2000), Cold spots in the Martian polar regions: Evidence of carbon dioxide depletion?, *Icarus*, *144*, 432–435, doi:10.1006/icar.1999.6302.

Wiscombe, W. J., and S. G. Warren (1980), A model for the spectral albedo of snow. I: Pure snow, *J. Atmos. Sci.*, *37*, 2712–2733, doi:10.1175/1520-0469(1980)037<2712:AMFTSA>2.0.CO;2.

Wolff, M. J., et al. (2006), Constraints on dust aerosols from the Mars Exploration Rovers using MGS overflights and Mini-TES, *J. Geophys. Res.*, *111*, E12S17, doi:10.1029/2006JE002786.

Wood, S. E. (1999), Nucleation and growth of carbon dioxide ice crystals in the Martian atmosphere, PhD thesis, 192 pp., Univ. of Calif., Los Angeles.